December 2014

Improving MRI Surface Coil Decoupling to Reduce B1 Distortion

Christian K. Larson
University of Wisconsin-Milwaukee

IMPROVING MRI SURFACE COIL DECOUPLING TO REDUCE B1 DISTORTION

by

Christian Larson

A Thesis Submitted in

Partial Fulfillment of the

Requirements for the Degree of

Master of Science

in Engineering

at

The University of Wisconsin-Milwaukee

December 2014

ABSTRACT

IMPROVING MRI SURFACE COIL DECOUPLING TO REDUCE B1 DISTORTION

by

Christian Larson

The University of Wisconsin-Milwaukee, 2014
Under the Supervision of Professor George W. Hanson

As clinical MRI systems continue to advance, larger focus is being given to image uniformity. Good image uniformity begins with generating uniform magnetic fields, which are easily distorted by induced currents on receive-only surface coils. It has become an industry standard to combat these induced currents by placing RF blocking networks on surface coils. This paper explores effect of blocking network impedance of phased array surface coils on B_1 distortion. It has been found and verified, that traditional approaches for blocking network design in complex phased arrays can leave undesirable B_1 distortions at 3 Tesla. The traditional approach of LC tank blocking is explored, but shifts from the idea that higher impedance equals better B_1 distortion at 3T. The result is a new design principle for a tank with a finite inductive reactance at the Larmor Frequency. The solution is demonstrated via simulation using a simple, single, large tuning loop. The same loop, along with a smaller loop, is used to derive the new design principle, which is then applied to a complex phased array structure.

TABLE OF CONTENTS

LIST OF FIGURES

LIST OF TABLES

ACKNOWLEDGMENTS

The author would first and foremost like to thank Dr. George Hanson for his guidance and flexibility in the completion of this thesis. The author would also like to extend the sincerest thanks to Dr. Saikat Saha, without whose technical guidance, this thesis would never have gotten past the first two chapters. Futher thanks are required to the author's employer for providing the funding for this research, a flexible work schedule, and the resources to complete it in a timely manner. Thanks are also required for Dr. Eddy Boskamp, Dr. Victor Taracila, and Dr. Saleka Bullamula who provided models, expertise, and guidance in understanding new physical principles. Dr. Ilya Avdeev and Dr. Chiu Law are extended the authors gratitude for agreeing to be comittee members. Finally the author would like to extend his sincerest thanks to his fiancée Jesse, for without her unwavering support, motivation, and understanding this work would not have been completed.

1 Introduction

As the field of Magnetic Resonance Imaging (MRI) advances, systems become more complex. One challenge faced by the engineers and physicist designing these systems, is the interactions between different portions of the systems, and the effect those interactions have on performance. As more imaging is done with localized surface coils, in order to obtain better local signal to noise ratios and resolution, the interactions between those coils becomes greater. As the phased array receive only coil has become in industry standard, the arrays have gotten more complex, and contain larger numbers of elements and denser structures. A result of the added complexity and density of the phased array, is a more complicated interaction and coupling to the system body coil. If the surface coil is not properly decoupled, undesirable distortion in the B_1 field will occur [1] .

2 Magnetic Resonance Imaging Background

2.1 MRI Physics Background.

With advances in the field of magnetic resonance imaging, 3 Tesla systems are being more widely used. Magnetic Resonance operates on the principle of exciting magnetic dipoles to spin, and using the received signal from those spinning magnetic dipoles to create an image. There are many steps that go into this process, which for the purposes of this work will largely be ignored, in order to keep the focus on the physics of the systems. In order to generate an MRI image there are three main magnetic fields at play which must be understood, the B_0 field (static main magnetic field), the B_1 field (time varying RF field that excites spins), and the gradient field (a much slower time varying field used to gain spatial information about the received signals).

An equation often used to describe the behavior of the magnetic dipoles, or net

magnetization vector (**M**), at a single location is the Bloch equation [2]

$$\frac{d\mathbf{M}}{dt} = \gamma\left(\mathbf{M}\times\mathbf{B}\right) - \left(\frac{M_x}{T_2}\mathbf{a}_i + \frac{M_y}{T_2}\mathbf{a}_j + \frac{M_z - M_o}{T_1}\mathbf{a}_k\right). \tag{1}$$

Here $\mathbf{a_i}$, $\mathbf{a_j}$, and $\mathbf{a_k}$ are the unit vectors in x, y, and z respectively. T1 and T2 are the longitudinal and transverse relaxation times.

The B_0 field strength is often used to describe an MRI system. In this case the system being studied is a 3T system, meaning the static magnetic field is 3 Tesla. The B_0 field is static, and the orientation of the field defines the coordinates system by defining the z-axis. An important relationship surrounding the B_0 field is the Larmor relationship [6]

$$\omega = \gamma B. \tag{2}$$

The Larmor relationship describes the natural frequency of the nuclear spin(ω) and its proportion to the static magnetic field **B**. γ is the gyromagnetic ratio, and often also referred to as the Larmor Frequency, and given in a ratio of $\frac{MHz}{T}$ [2]. Unless being used for spectroscopy, the MR system is generally used to image hydrogen, which has a Larmor frequency of $\gamma = 42.576$ MHz [4]. At 3 Tesla, this gives a natural frequency of f_0= 127.72 MHz. Any spin that is excited in the plane transverse (x,y plane) to the B_0 field, will precess at its natural frequency around the B_0 field (z-axis). A precessing magnetic dipole generates a signal that can be picked by an RF receiver.

The B_1 field, which is used to excite spins, will be the the main focus of this work. The B_1 field is a polarized RF field used to excite the spin of the protons, and is applied in the plane transverse to the B_0 field. Generally the B_1 field is circulary polarized in the x-y plane, and for our purposes is driven by RF pulse at the 3T Larmor frequency, and can be described by

$$B_{1x} = B_1\cos(\omega t) \tag{3}$$

$$B_{1y} = -B_1\sin(\omega t). \tag{4}$$

When driven at the Larmor Frequency the total applied B field can be written as

$$B(t) = \begin{bmatrix} B_1 \cos(\omega_o t) \\ -B_1 \sin(\omega_o t) \\ B_0 \end{bmatrix}. \tag{5}$$

By looking at the B field in a rotating reference frame (that is rotating at the Larmor frequency) , the circularly polarized B_1 field can be looked as constant both in orientation and magnitude [2].

Another important factor to be considered in MR physics is the flip angle. For the purposes of this work, the flip angle will always be considered to be transverse to the B_0 field (90° flip angle). In reality different flip angles are desirable depending on the imaging being done. The flip angle and RF field strength are related as [3]

$$\theta = \gamma B_1 \tau. \tag{6}$$

Here B_1 is the RF field magnitude, and τ is the RF pulse duration. Ideally this flip angle would be constant across the entire imaging volume of interest, however non-uniformities will cause the flip angle at a specific position to deviate from (6), and can be described by the adjusted flip angle θ_a [3]

$$\theta_a(r) = \zeta \theta_n. \tag{7}$$

In (7), ς is the the scaling factor for B_1 at position (r). In a uniform sample, a uniform flip angle across the sample would return a uniform signal intensity across the sample. In order to generate a uniform flip angle as described in (6), a uniform B_1 field is required across the imaging sample. If the flip angle varies as described in (7), there will be varying signal intensities across a uniform sample, which is non-desirable. This drives the requirement in MRI systems to generate the most homogeneous B_1 field possible. This becomes more difficult as field increases, since B_1 homogeneity worsens as B_0 strength increases [3]. In

most systems the B_1 transmit field is generated by a volume resonator, or volume coil, in this case also referred to as the body coil.

2.2 Body Coil Design Background

Volume resonators, and body coils specifically, come in many different sizes and topologies including saddle coils, TEM coils, and birdcage coils. Birdcage coils are the most popular topology for body coils today due to their high B_1 homogeneity [5][6]. Birdcage resonators themselves come in several different topologies including low-pass, band-pass, and high-pass. Birdcage coils are designed to consist of two circular end rings at either end of the coil, with conductive strips connecting the end rings to each other as shown in Figure 1 below. The conductive strips are often referred to as the "legs" or "rungs" of the birdcage.

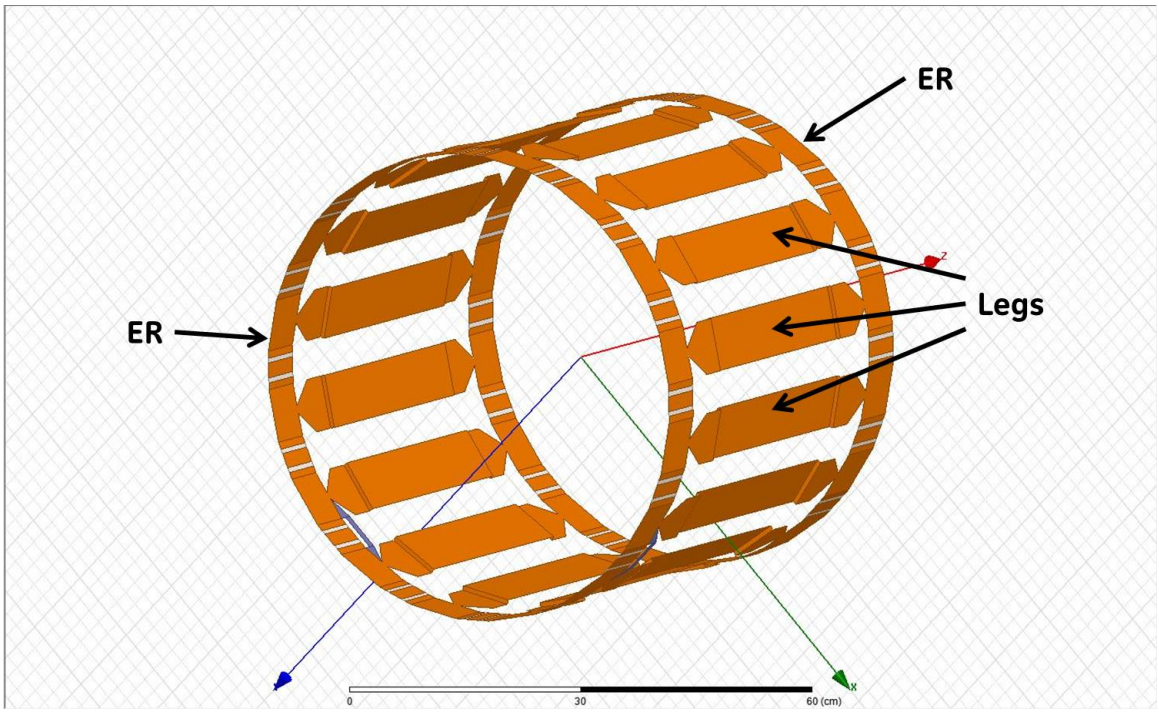

Figure 1: Birdcage Body Coil Geometry.

The difference between and high pass and low pass birdcage topology are the location of the capacitors. For a high-pass birdcage the capacitors are located on the end rings, and placed between the rungs of the birdcage. Conversely for the low-pass birdcage the

capacitors are located at the center of each rung, while the end rings remain inductive [5][6]. The birdcage design is based on the principle that a transverse magnetic field is generated by an axial current, with a distribution one sinusoidal cycle around the wall defined by the birdcage cylinder. This current is defined by (8), where θ is the azimuthal angle of the cylinder [6]

$$I = I_o \cos(\theta). \tag{8}$$

As can be seen in Figure 1 the birdcage is not a continuous cylindrical sheet, but rather approximates one with evenly distributed rungs around the cylinder. With this approximation, the coil becomes an LC ladder filter with the capacitance and inductance adjusted to achieve a phase shift of 2π in the voltage around the circumference of the end ring. Simple circuit analysis shows that a sinusoidally varying voltage on the end ring will create a sinusoidally varying current on the rungs of the birdcage. It is the magnetic fields generated by the rungs of the coil that add to give a homogeneous B_1 field. The size of the homogenous region of B_1 is determined by how well the current distribution on the rungs of the birdcage approximate a continuous current on a "cylindrical sheet" [6]. The detailed analysis for obtaining the resonance conditions for the LC ladder network is presented in [6], and summarized by

$$\omega_o = \frac{1}{2\sqrt{LC}\sin\left(\frac{\pi}{N}\right)} \tag{9}$$

$$\omega_o = \frac{2}{\sqrt{LC}}\sin\left(\frac{\pi}{N}\right). \tag{10}$$

With (9) and (10) representing a high-pass and low-pass birdcage respectively, where N is the number of rungs. If the coil is long enough, the field geometries at iso-center will be determined solely by the current on the rungs. In fact a perfectly homogeneous B_1 field is possible if the coil is infinitely long. However, in practice an infinitely long coil is not possible and there must be some current return path [11]. For the purposes of this work,

the actual coil geometries of the design, and resulting field properties will be detailed in Chapter 3.

2.3 Surface Coil Background

Surface coils come in many different topologies, geometries and form factors, but are generally broken down into two different categories: Transmit-Receive coils, and Receive-only coils. Surface coils sit closer to the sample being imaged than the body coil, and therefore can provide much higher signal to noise ratios, and improved image resolution. Generally, a receive coil is a resonant (inductive) loop, tuned using distributed capacitors along its perimeter. For the purposes of this paper, the focus will be on receive only coils, and more specifically phased array coils. A phased array coil is an array of multiple receiving loops, designed to simultaneously receive signal from the sample being imaged, an example geometry is shown in Figure 2.

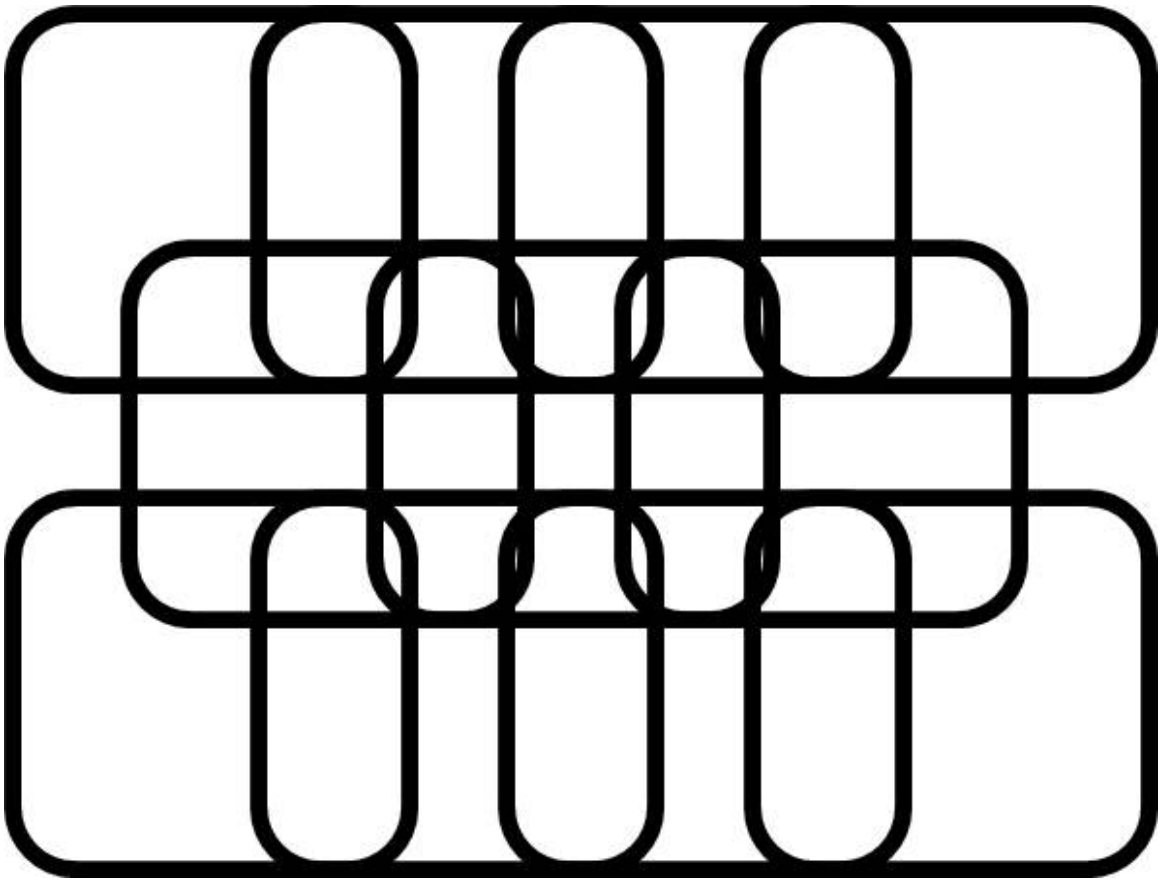

Figure 2: Generic phased array receive coil structure.

This work will not go into the details of surface coil design, but rather focus on the single aspect of decoupling surface coils during RF transmit by the body coil. Vaughan's "RF Coils for MRI" gives a good overview for surface coil design [7]. During RF transmit by the body coil, general practice is to detune the receive coils in the system in order to minimize the current induced in the receive coil, which can contribute to B_1 inhomogeneities [1][8][9][10]. A resonant loop placed into a time varying B_1 field will have a voltage induced along its perimeter, which can be described by [8]

$$E_{emf} = -\delta_t \iint \mathbf{B}_1 d\mathbf{S}. \tag{11}$$

Ohm's law then dictates that the induced current in the loop will be an effect of this

voltage, and the impedance of the loop will be

$$I_{loop} = \frac{E_{emf}}{Z_{loop}} \tag{12}$$

where Z is complex.

Since B_1 is a time varying magnetic field, the current induced in the loop is time varying, which in turn generates another magnetic field [8]. Since a volume resonator is designed to produce a homogenous B_1 field when empty, the presence of an inadequately decoupled surface loop will cause inhomogeneities in B_1 via the secondary field generated by the induced current. In order to reduce the issue described above, standard practice is to increase the impedance of the loop during body coil transmit, in order to reduce the induced current in the loop.

There are several different methods for increasing the loop impedance during transmit, and go back to resonating during the receive mode. The first method is what is referred to as a passive blocking network, which gets its name because is it self-activating during RF pulsing. This is accomplished by placing an inductor in parallel with one of the distributed capacitors to create an LC tank, which is resonant at the Larmor frequency. The inductor is switched in and out of the circuit using parallel diodes which are biased by the RF pulsing [1]. An example of this circuit is shown in Figure 3 below [7].

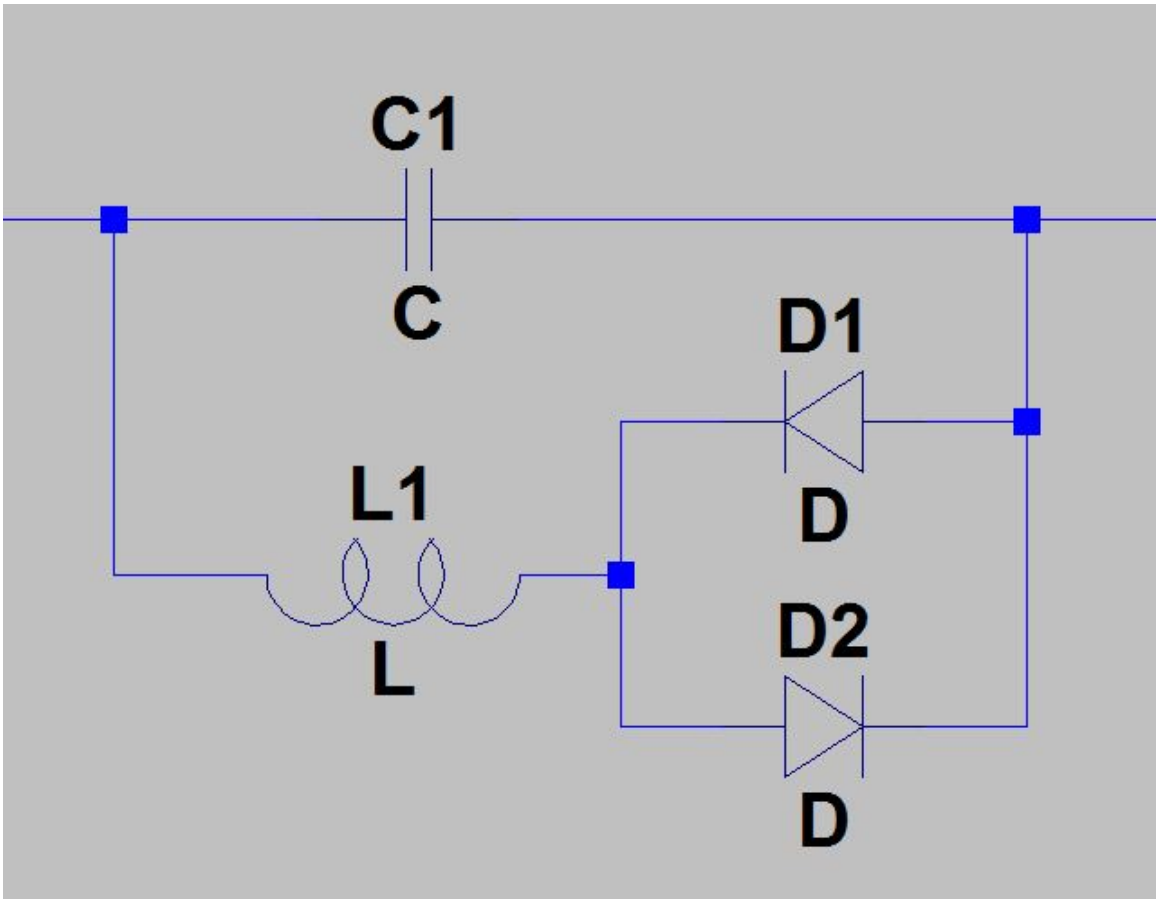

Figure 3: Passive detuning circuit using parallel LC tank.

The second type of detuning circuit is an active blocking network. It is similar to the passive circuit in that it again uses an LC tank resonating at the Larmor frequency, but uses a pin diodes biased by a DC signal. This allows for greater timing control of the detuning circuit. The final type of decoupling circuit is a hybrid decoupling presented in [9].

Since inadequate detuning, or inadequate blocking, can result in secondary B fields, causing B_1 inhomogeneities, rules for quantifying necessary blocking are highly desired. In [1] an experimental analysis is done in a GE Healthcare system to determine necessary blocking impedances. Kochorian et al [10] performed a more rigorous experiment, which varied loop size to asses its impact on blocking impedance. Additionally Kochorian et al developed a method to assess the impact of inadequate blocking on image quality.

Finally Taracila et al produced a design rule via analytical analysis to determine necessary blocking to keep B_1 distortions under 5% [8].

3 Problem Demonstration

3.1 Body Coil Design Details

For the remainder of this work the body coil being referenced will be a 3.0T high pass birdcage. Generally in an MR system the body coil is surrounded by an RF shield to protect the coil from outside noise generated by the gradient coil and superconducting magnet [5]. In most systems the body coil end rings and legs lie on one cylindrical surfaces, as shown in Figure 4.

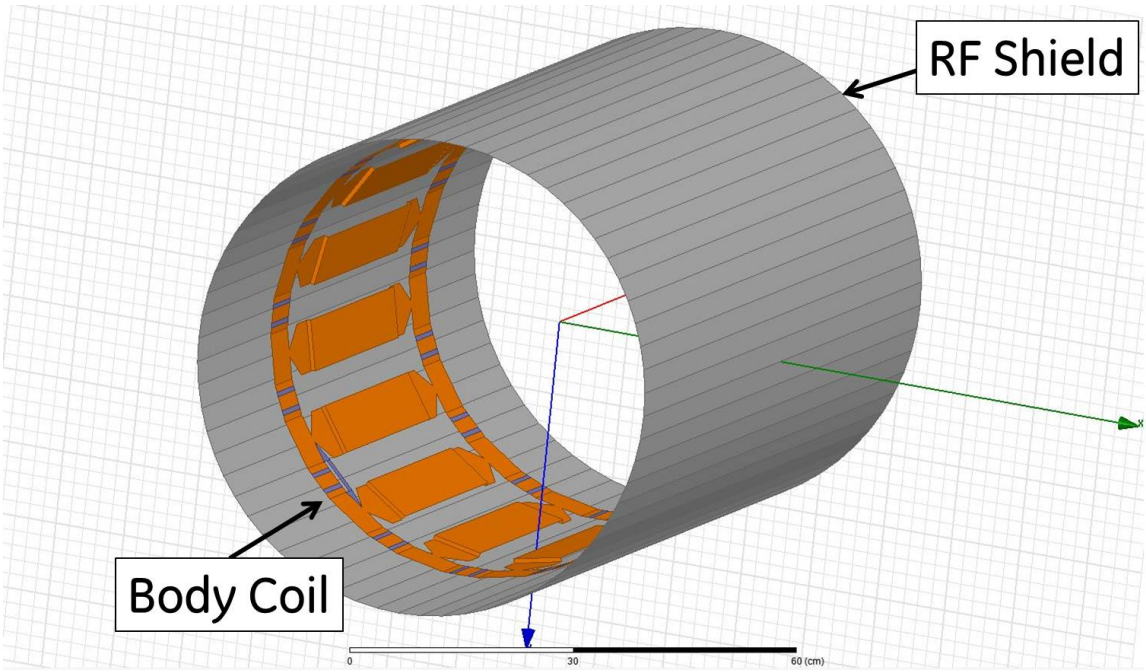

Figure 4: High pass birdcage and RF shield.

Additionally the body coil has two drive points on what is referred to as the service end, end ring shown in Figure 5 below. The drive points are located 90° out of phase and driven with cosine wave phase shifted by 90° on one of the ports.

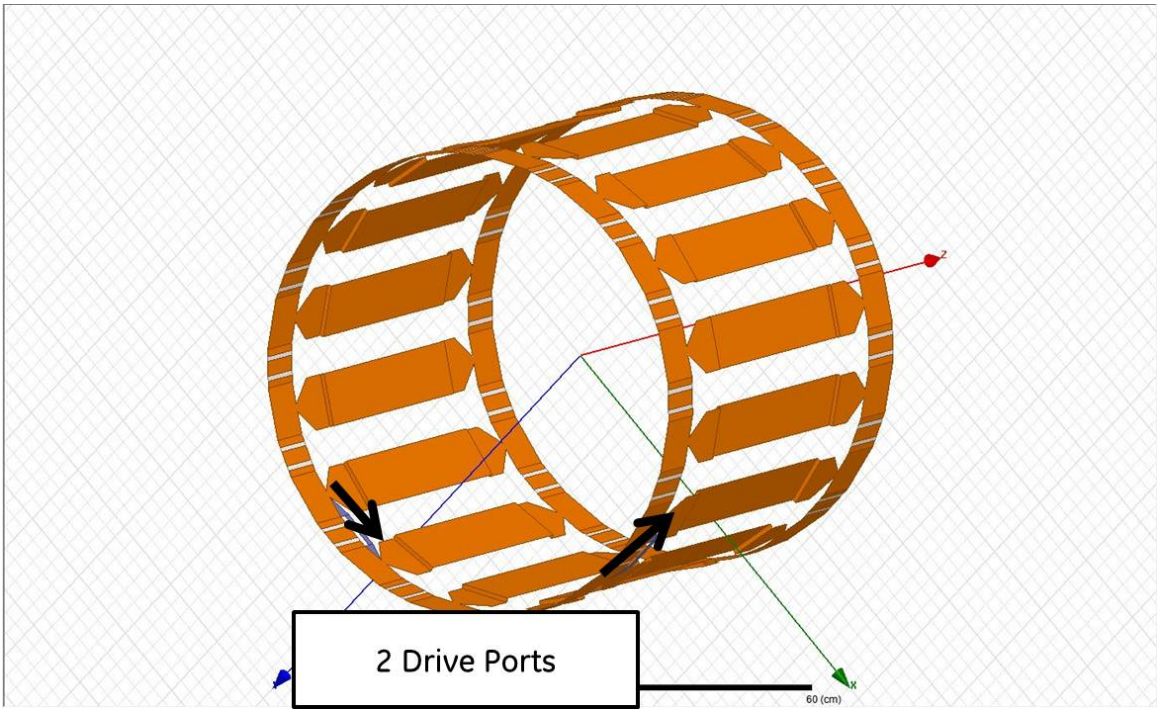

Figure 5: Body Coil Drive Scheme.

The body coil is a 16 rung birdcage with an overall length of 560mm from end to end. As discussed above the coil has two different diameters between the legs and the end rings. There are two capacitors in series between each rung, the capacitor locations are shown in Figure 6.

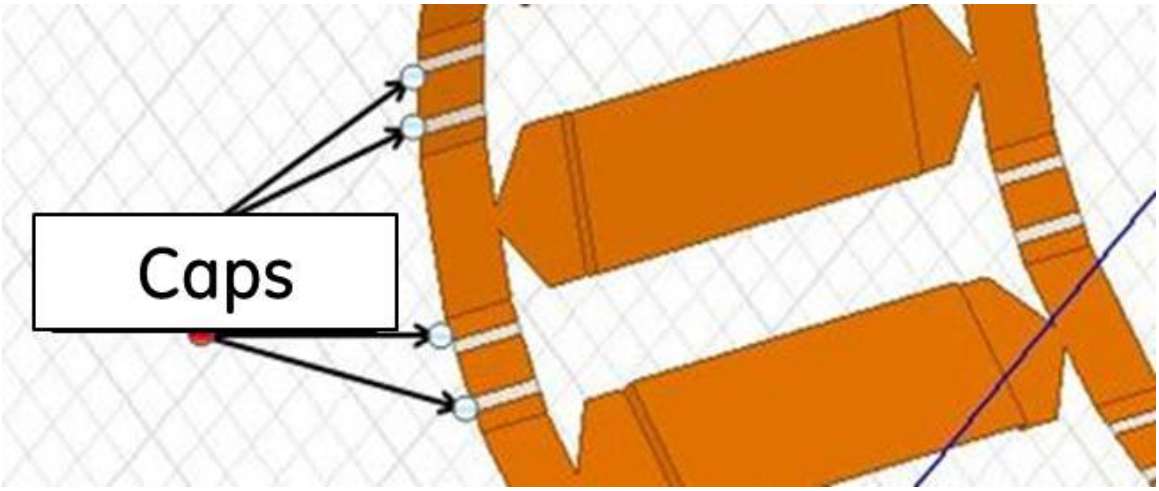

Figure 6: High pass birdcage capacitor locations.

3.2 Body Coil Performance Parameters

There are several parameters on which the body coil performance is measured to demonstrate performance, and will be detailed in this section. The body coil as described above was modeled in ANSYS HFSS, as well as constructed in the lab which will allow for the comparison of the model to real life measurements.

The first step in ensuring coil performance both in simulation, and in the lab, is to tune the coil, which is performed using a two probe tuning method. This tuning method involves placing two coplanar broad-band tuning loops opposite each other in the body coil, at the z=0 point, and measuring the frequency at which the probes most strongly couple. There is also a loop tuned to the Larmor frequency oriented orthogonally to the two tuning loops in order to short out the orthogonal mode of the body coil. The probes are then rotated to positions every 22.5 degrees around the coil to make sure each azimuthal position is similar. A photo of the tuning setup can be seen in Figure 7 below, while Figure 8 shows the S21 output on the network analyzer for the vertical mode being measured.

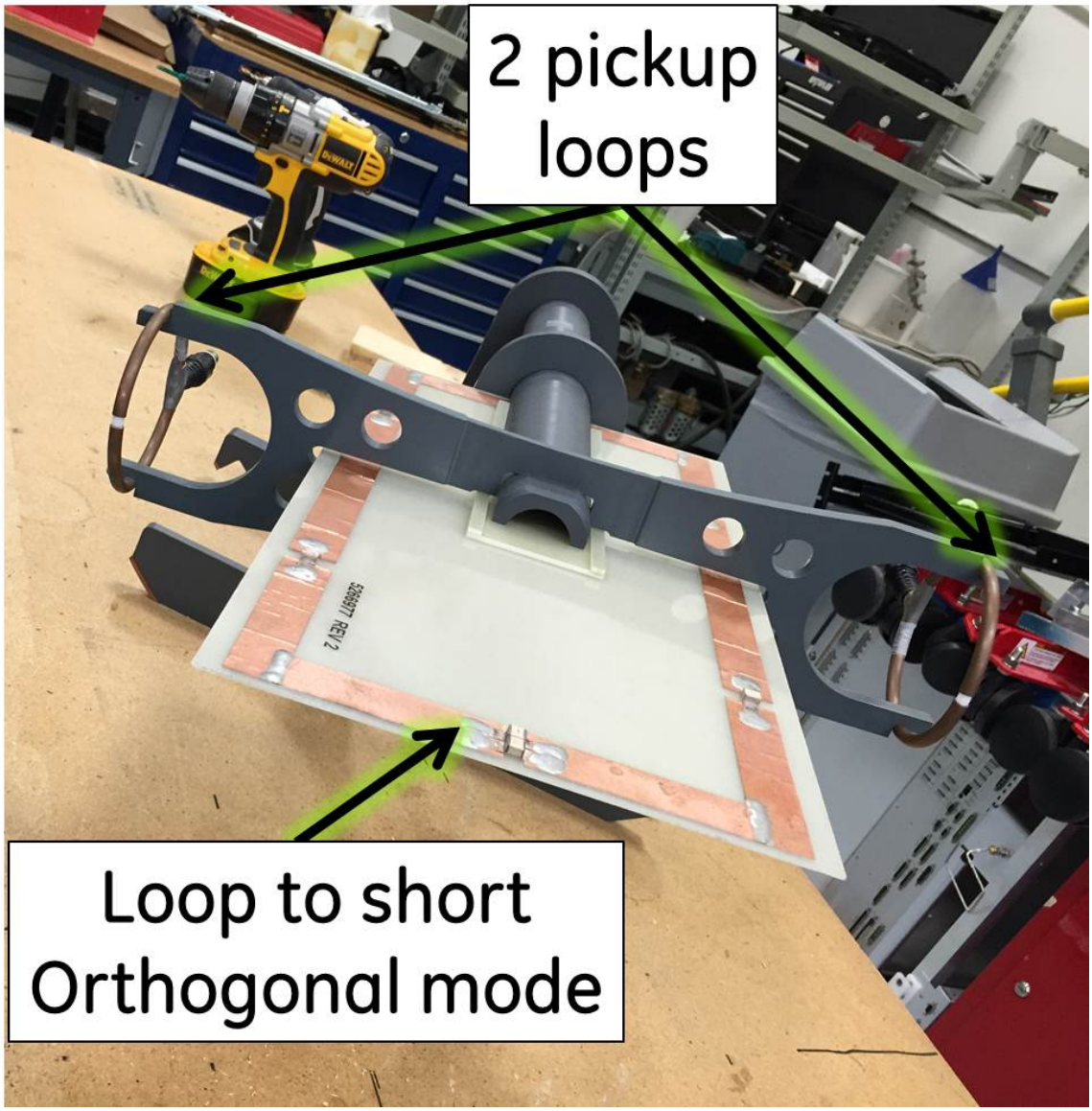

Figure 7: Two probe tuning fixture for body coil tuning.

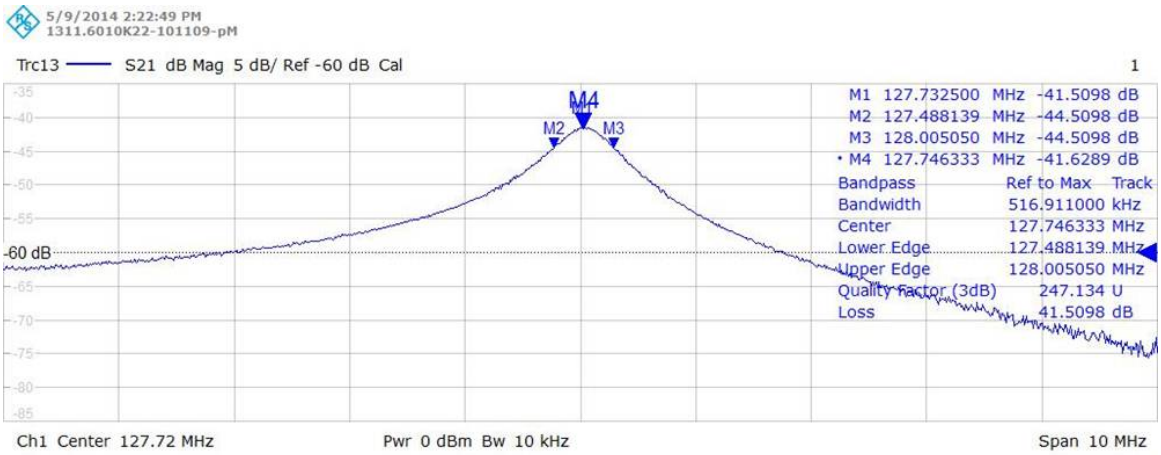

Figure 8: Vertical mode S21 from body coil tuning probes.

As detailed in Section 2 the Larmor frequency of interest for a 3.0T system is 127.72 MHz. Therefore the desire is for each of the eight modes to be tuned as tightly to 127.72 MHz as possible. Table 1 below shows the tuning frequency of each mode as measured in the simulation as well as in the lab. The angle of the measurement is the azimuthal angle from vertical. The measurements demonstrate there is agreement between the simulation and the prototype coil. Additionally the table shows that the tuning is very balanced between each mode in the model.

Measurement Angle (deg)	Model f_o(MHz)	Lab f_o(MHz)	Difference (MHz)
0	127.42	127.75	0.33
22.5	127.4	127.72	0.32
45	127.43	127.71	0.28
67.5	127.4	127.73	0.33
90	127.43	127.77	0.34
112.5	127.4	127.81	0.41
135	127.44	127.80	0.36
157.5	127.4	127.78	0.38

Table 1: 2 Probe Tuning Measurements

The next tuning step is to check for agreement in the S-parameters for the coil itself. As was discussed before there are two drive ports on the coil, which allows the use of two port analysis to be used. For the simulation and lab measurements the S11, S22, and

S21 parameters will be considered. Figure 9 and Figure 10 below show the simulation S-parameters and lab measured S-parameters respectively. The details of the S-parameters are shown in Table 2, which demonstrate the input matching is better in the actual coil, and so is the isolation. However the model shows that the inputs resonate at the same frequency as the two probe measurement.

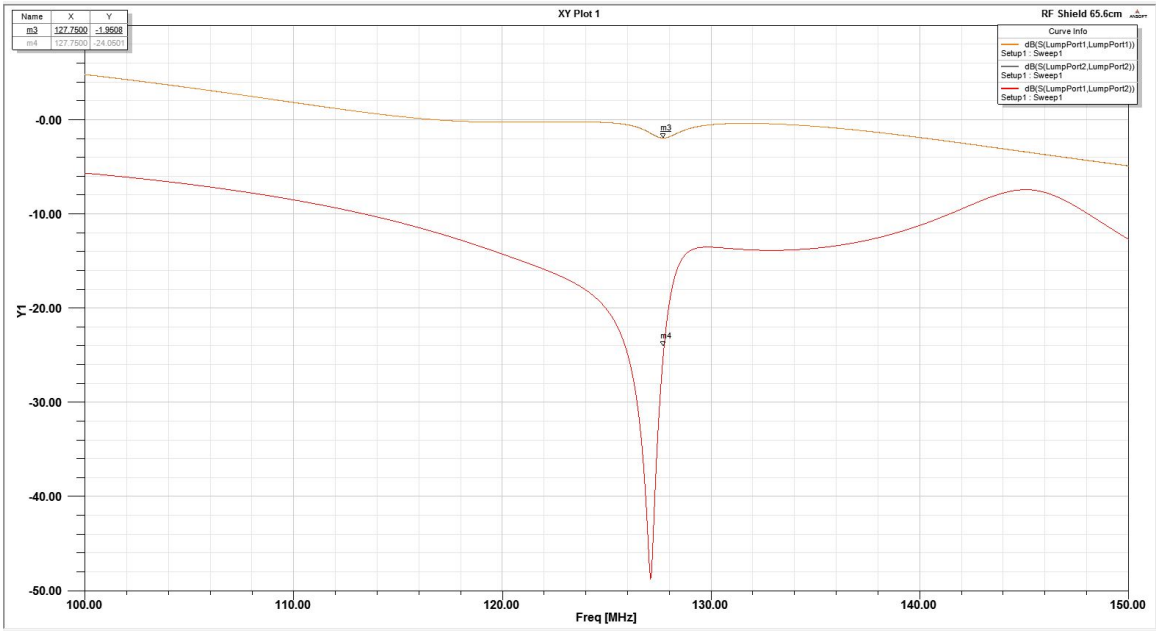

Figure 9: S-parameters from HFSS model.

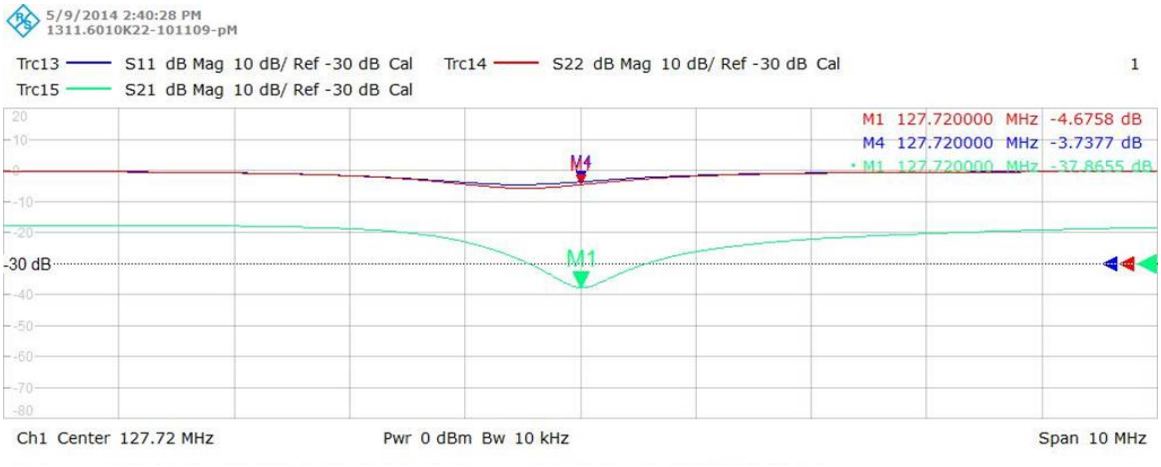

Figure 10: S-parameters measured on prototype body coil.

	Model	Model	Measured	Measured
	f_o(MHz)	Magnitude @ 127.72MHz (dB)	f_o(MHz)	Magnitude @ 127.72MHz (dB)
S11	127.75	-1.95	127.18	-3.74
S22	127.75	-1.95	127.22	-4.47
S21	127.2	-24	127.75	-37.86

Table 2: S-Parameters: Magnitude and resonant frequency for body coil model and body coil prototype.

The E field distributions are shown in Figure 11 below for the axial, sagittal, and coronal planes respectively. The plots show a balanced distribution, with the highest fields at the end rings of the coil. Additionally, the current distributions in Figure 11 show relatively balanced current on each rung. If closely inspected it can be seen one end ring carrying slightly more current than the other, which is reflected with slightly higher fields at one end ring. This will become more evident in the B_1 plots shown in Figure 12.

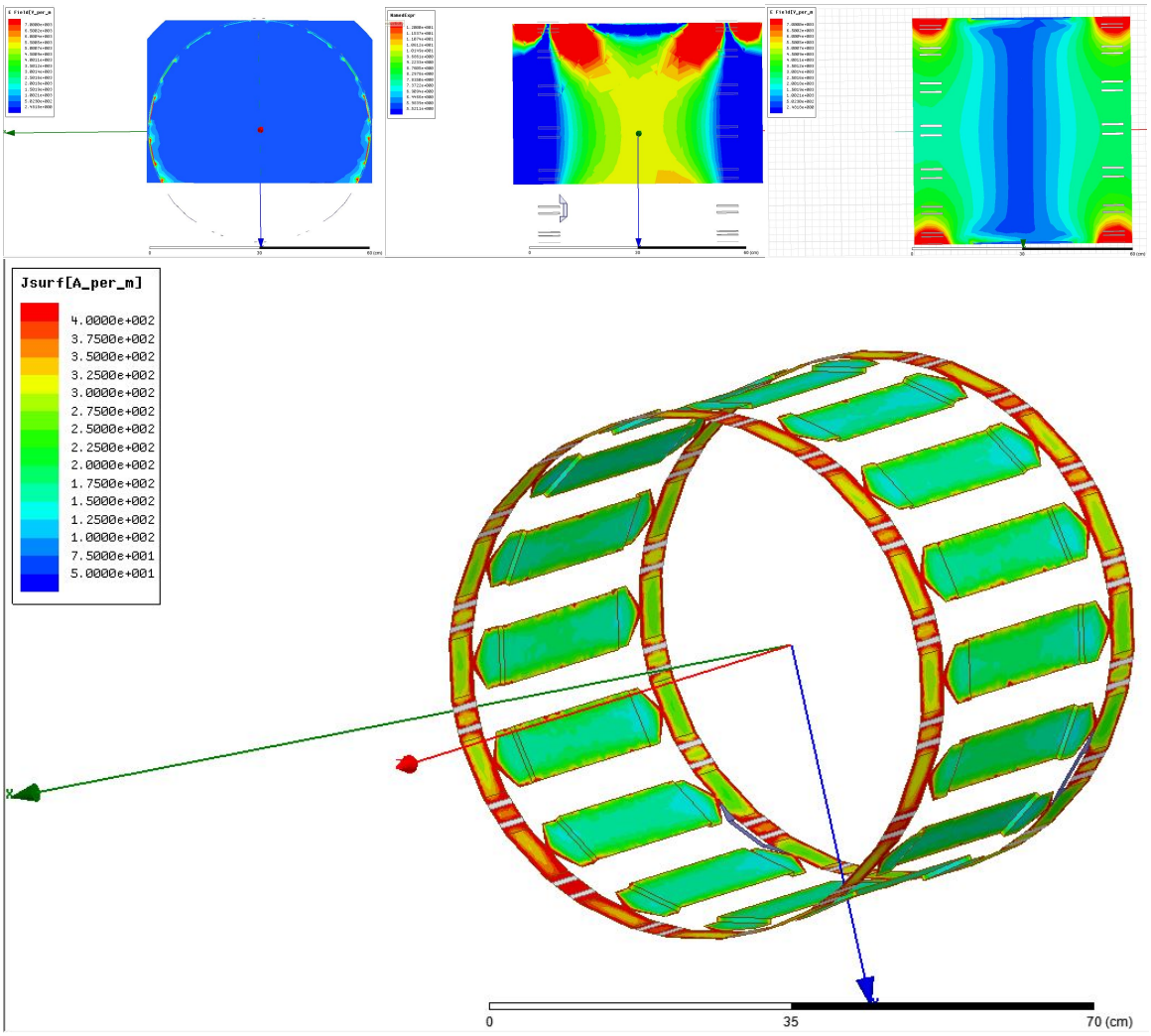

Figure 11: E-Field and current distributions for body coil model.

The main parameters of interest for this work are the B_1 parameters. Figure 12 below shows the B_1 distribution across the main planes of interest; axial and sagittal respectively in the first row. The second row shows two different coronal planes, first located at iso-center. The second located in what is defined as the surface coil coronal plane, which is ~14.5 cm below iso-center. The importance of the second coronal plane becomes important when a surface coil is introduced near the plane. More detail about the plane will be given later. As shown in Figure 12, the fields are well centered and relatively homogeneous over the imaging volume at iso-center, with slightly higher fields near the end ring carrying more current discussed above. As a side note the axial and sagittal

planes do not extend all the way to the bottom of the coil as the patient table and other pieces of the system occupy this region, and therefore it is not of interest.

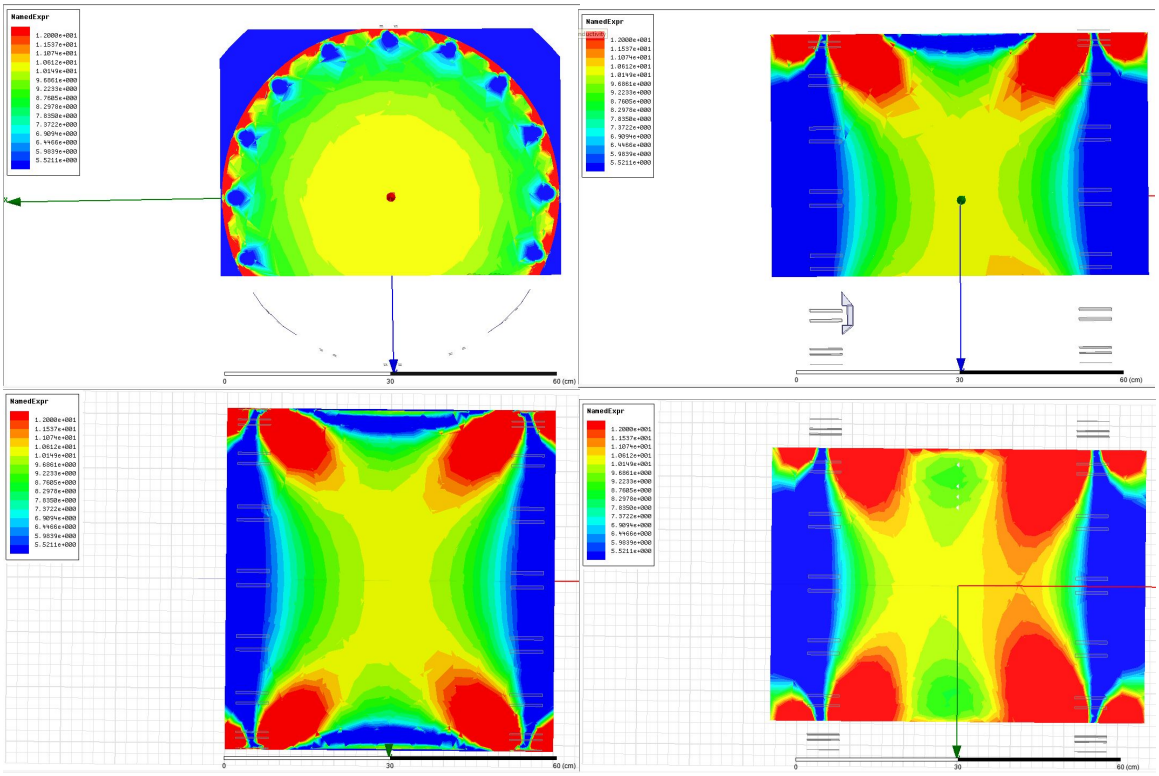

Figure 12: B_1 field maps for empty body coil model.

For the purposes of this work, a quantification of B_1 homogeneity was for the planes of interest. There are several different methods which could be used, however The Association of Electrical Equipment and Medical Imaging Manufacturers, from here on referred to as NEMA, Peak Deviation Non-Uniformity (PDNU) method will be used [12]

$$N = 100\frac{Smax + Smin}{Smax - Smin}. \tag{13}$$

The NEMA Standards Publication "Determination of Image Uniformity in Diagnostic Magnetic Resonance Images" provides methods for calculating MR image non-uniformities. Since the B_1 transmit field uniformity is directly related to the received signal, and image quality, the same methods can be used to evaluate the field homogeneity. Additionally,

the other methods provided in the NEMA standard are used to reduce image noise before calculating uniformities. However, since only B_1 transmit is being considered, noise reduction, and noise contribution is not a concern, therefore the Peak Deviation Non-Uniformity was chosen as the best parameter for measuring B_1 homogeneity. For the interest of this work, the homogeneity in the coronal plane will be most important, for reasons that will become clear in Section 3.4

Since the NEMA PDNU equation is written as a non-uniformity, if homogeneity (uniformity) is the parameter of interest, it can be rewritten as (14), and simplified into (15) below, which will be referred to as the modified NEMA PDNU from here on.

$$U = 1 - N \tag{14}$$

$$U = \frac{200}{1 + \frac{Smax}{Smin}} \tag{15}$$

For the purposes of this experiment a 40cm by 42cm rectangle, centered at iso-center and placed in the XZ plane was chosen as the measured region of interest. Since the measurement is a ratio, it remains constant despite changes in drive power to the coil, but for consistency sake the drive power was kept at 1000 watts per drive, or 2000 watts total. Figure 12 above shows what the field distribution on this plane looks like at the specified drive power, and (15) produced a uniformity of 65.2% and drives 11 uT at iso-center.

3.3 Surface Coil Design Details

In Section 2, the background of surface coils, and specifically phased array receive coils was given. The surface coil used in this work is a fixed position receive only phased array with a combination of single loops and butterfly receivers, along with its receive circuitry. The surface area of the loop geometries are given in Table 3.

	Loop 1	Loop 2	Butterfly
Area (cm^2)	129.3	163.8	244

Table 3: Surface coil surface area per loop.

The surface coil receiver loops have two decoupling circuits per loop. The decoupling circuits are parallel LC resonant tanks tuned to the Larmor frequency of 127.72MHz. In the system the surface coil is positioned such that the loops are 15 cm below iso-center as shown in Figure 13.

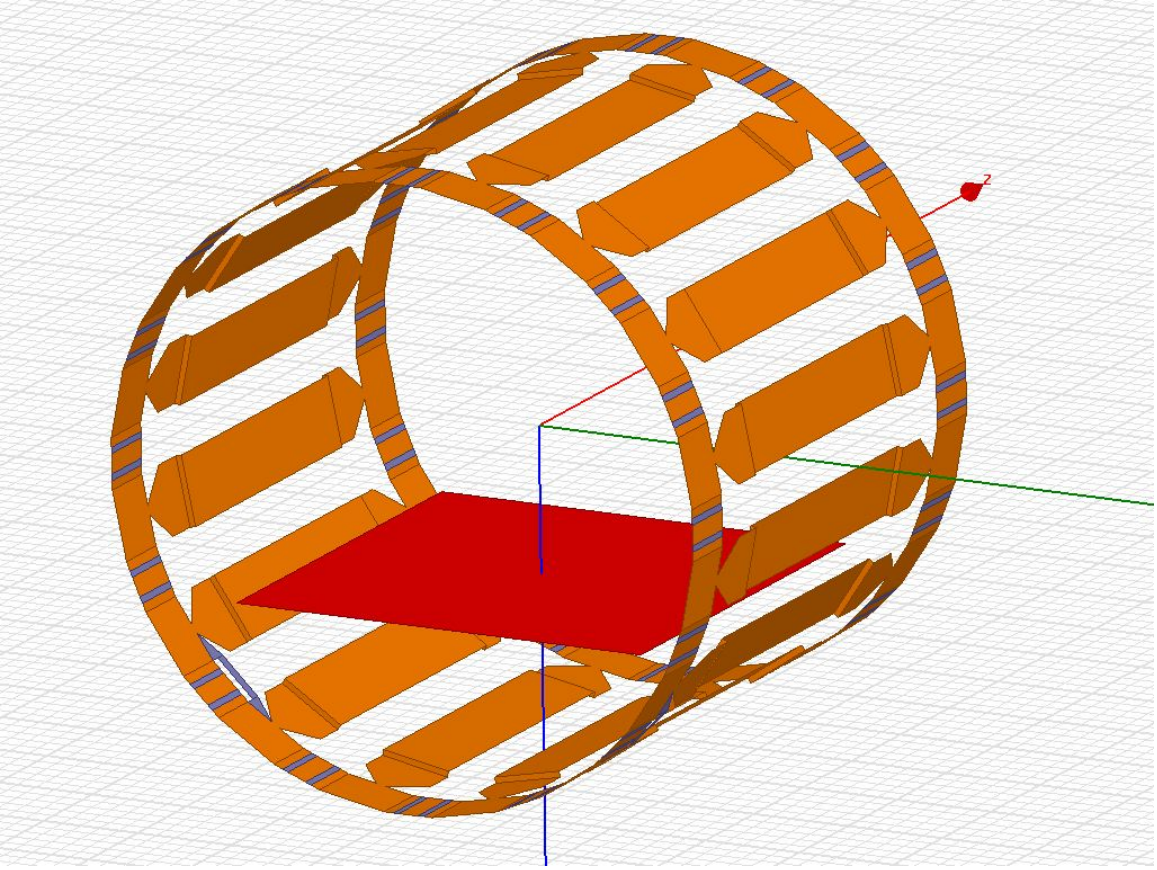

Figure 13: Surface coil position in body coil, 15cm below iso-center.

3.4 Surface Coil Body Coil Interactions

Once the surface coil is placed into the body coil there are several impacts to the body coil. It is very important to emphasize here that we are looking at the surface coil in the

"decoupled" state, or with its blocks activated to high impedance, for the remainder of this paper. This is because we are interested in the non-uniformities in the B_1 transmit field generated by the body coil. The impact of most interest is the B_1 non-uniformity, however the easiest to measure is the tuning impact, which will be looked at first. The largest tuning impact is to the vertical mode of the body coil, however every mode is impacted as detailed in Table 4, as measured in the lab.

	Empty f_o(MHz)	Surface coil Present f_o(MHz)	Difference f_o(MHz)
0	127.75	127.48	-0.27
22.5	127.72	127.48	-0.24
45	127.71	127.54	-0.17
67.5	127.73	127.63	-0.1
90	127.77	127.67	-0.1
112.5	127.81	127.67	-0.14
135	127.80	127.66	-0.13
157.5	127.78	127.58	-0.2

Table 4: Tuning impact of surface coil presence versus empty body coil by varied azimuthal measuring angle.

Figure 14 below shows the frequency shift versus angular position according to (16) with the radial scale given in MHz.

$$f(\theta) = f_{o_{empty}}(\theta) - f_{o_{SC}}(\theta) \tag{16}$$

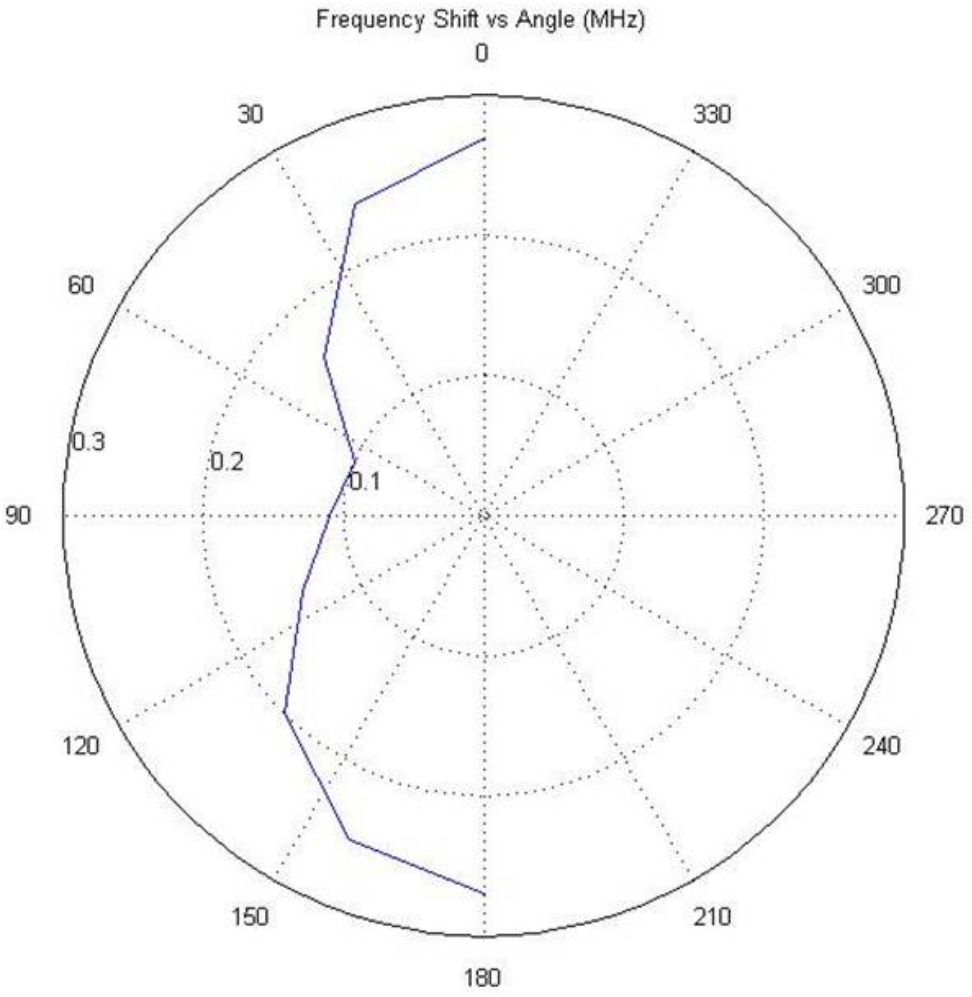

Figure 14: Resonant frequency shift in surface coil presence from empty body coil vs azimuthal measurement angle.

There are also tuning impacts to the S-parameters, as shown in Figure 15. The largest impact is to the measured isolation between the two ports, or the S21 parameter, which is reduced from -37.86dB to -18.7dB at 127.72MHz. This indicates that the ports are now coupling relatively well through the surface coil coil, even when it is in the decoupled state.

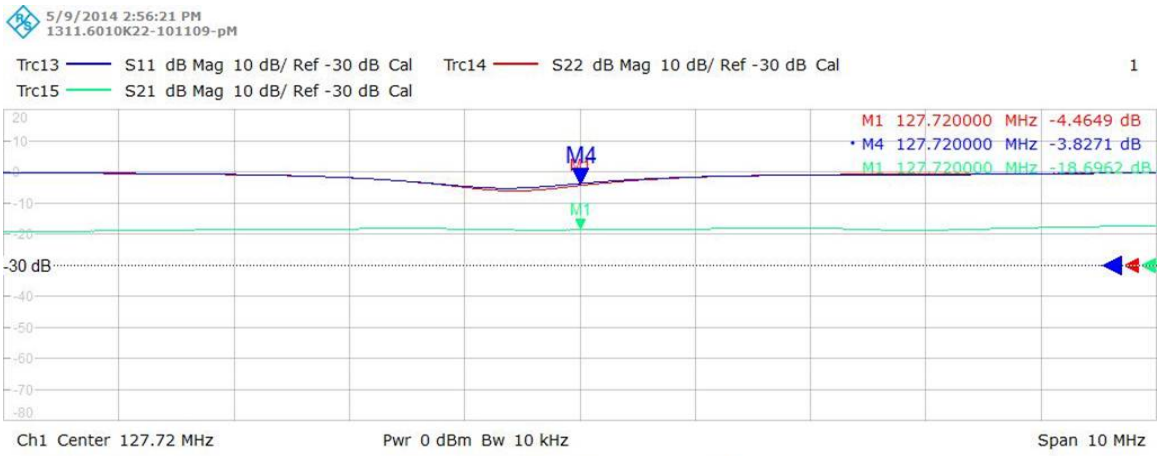

Figure 15: Lab measured S-parameters with surface coil present.

The impact to be focused on is the impact to the B_1 uniformity. While the surface coil doesn't have a large impact in the coronal plane at iso-center, it does have an impact in the sagittal plane, axial plane, and the largest impact in the coronal plane just above the coil surface. Figure 16 gives a good qualitative image of the distortions to the axial, sagittal, and coronal fields at iso-center when the decoupled surface coil is introduced. It is noted that the axial and sagittal planes both show large disturbances near the surface coil surface. These are caused by the secondary fields adding to the B_1 fields generated by the body coil.

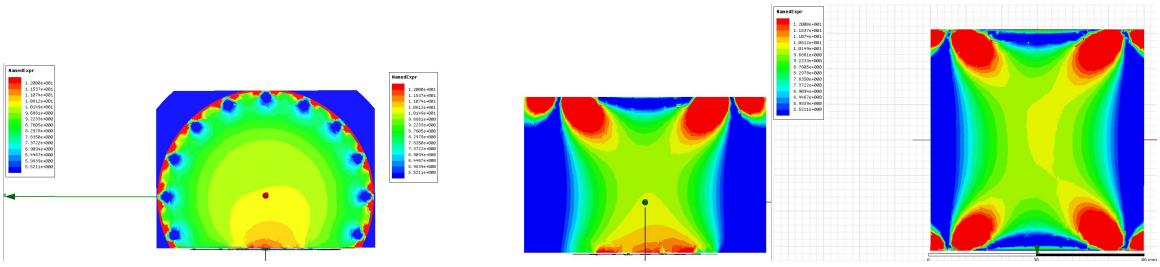

Figure 16: B_1 field maps with surface coil present, showing the axial, sagittal, and coronal planes at iso-center.

The problem with looking at the axial and sagittal slices is that they are orthogonal to the surface coil. Looking at the coronal plane just above the surface coil provides the greatest insight the non-uniformities introduced by the secondary fields. The surface coil

coronal plane as defined in Section 3.2 is defined as the plane parallel to the surface coil loops, and sitting 5 mm above the coil surface, with the same dimensions as the coronal plane at iso-center. For ease of comparison Figure 17 shows the B_1 in the surface coil coronal plane, first in the empty condition, then in the presence of the surface coil. It is incredibly clear the disturbance in the plane is caused by the surface coil presence.

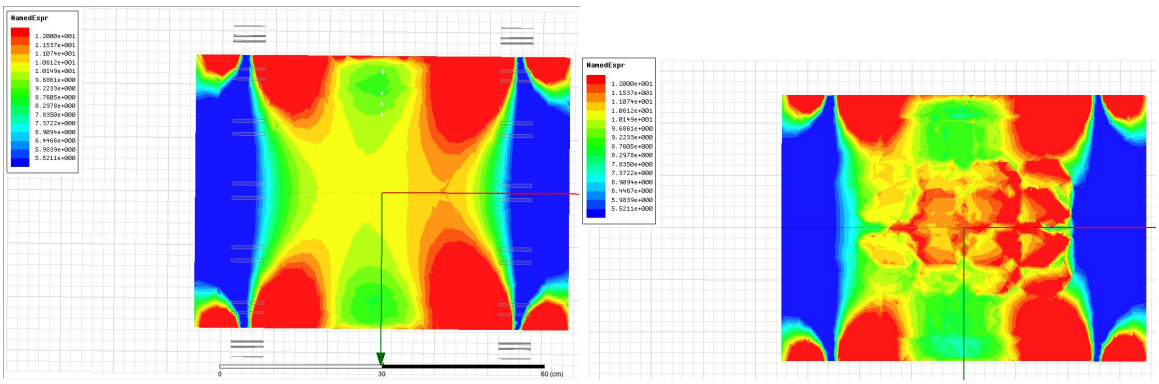

Figure 17: B_1 field in the surface coil coronal plane in the empty condition and with the surface coil present.

Again the modified NEMA PDNU (15), can be used to define uniformity for the empty and surface coil present conditions as shown in Table 5 below [12]. The reduction in uniformity in the empty condition is seen because the plane dimensions didn't change, but moved down in space. This brings it closer to the end rings of the bird-cage, causing higher fields at that location, while the minimum seen near the plane edge in other locations remains similar. However the surface coil presence still reduces the uniformity in the plane by 13%.

	Empty(%)	Surface Coil Present(%)
PDNU	43.4115	30.3856

Table 5: Modified NEMA PDNU measured in the surface coil coronal plane, for the empty and surface coil present conditions.

4 Solution Theory

4.1 Inductive Blocking Introduction

It is clear from the previous section that the surface coil has an undesirable effect on B_1 homogeneity. Taracila et al, who provided the most comprehensive paper on recommended blocking impedance, would recommend a minimum impedance for each loop as shown in Table 6 per (17), where S is the area occupied by the loop [8].

$$\left.\frac{|Z_l|\,[ohm]}{S\,[cm^2]}\right|_{5\%} \approx \frac{1}{4} f_o\,[MHz] \tag{17}$$

Loop	Size (cm^2)	Recommended Z_l(ohms)	Actual Z_l(ohms)
Loop 1	129.3	4128.55	~2x10^6
Loop 2	163.8	5230.13	~2x10^6
Butterfly	244	7790.92	~2x10^6

Table 6: Recommended minimum blocking value and actual implemented blocking value.

As is easily seen in Table 6 the blocking impedance per loop vastly exceeds the recommendation, yet there are still uniformity issues observed. This is believed to be due to the complicated structure of the phased array coil. As the structures grow more complicated, the number of capacitive overlaps increase, which cause unaccounted for current loops to form within the phased array structure [13]. This indicates that in a structure like this, induced currents in individual loops can be minimized, but overall surface currents cannot be eliminated, and therefore must be managed in a way that minimizes their contribution to B_1 distortion.

If a receive only loop in the body coil is treated as a resonant coupled circuit, shown in Figure 18, Kirkhoff's Law can be used to derive the relationship for the induced current [14]. If the second loop has an inductive impedance, Kirkhoff's Law shows that the induced current will be 180° out of phase with the excitation current, as shown in (18).

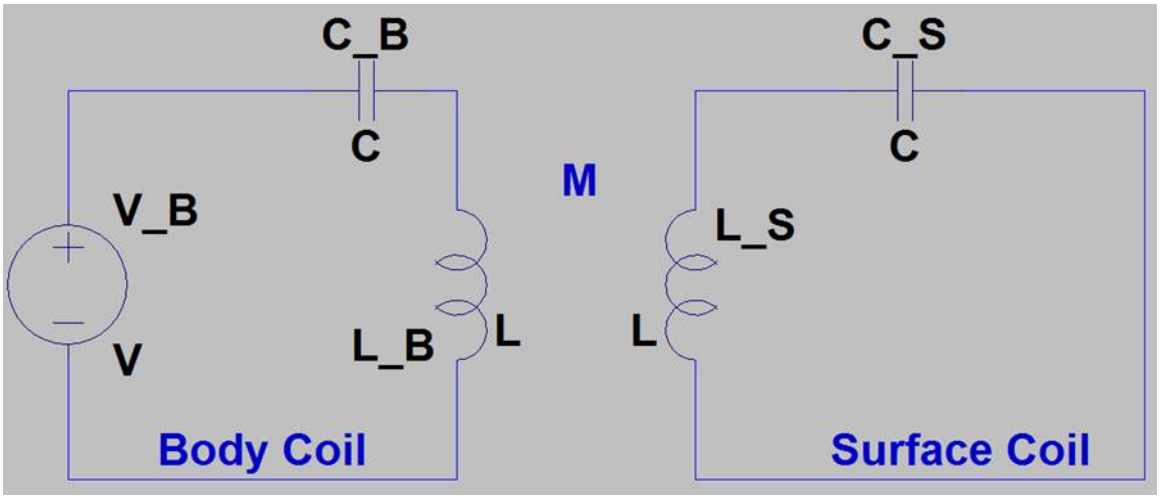

Figure 18: Resonant coupled circuit model.

$$i_s = -i_b \left| \frac{X_m}{X_{CS} + X_{LS}} \right| \tag{18}$$

Conversely, if the loop has a capacitive impedance, the current will be in phase with the excitation current. If the induced current is in phase with the excitation current, the secondary B field will be in the same direction as the B_1 field, and therefore result in a higher B_1 local to the induced current.

4.2 Large Loop Experiment

In order to verify the above theory in a simpler structure before applying to the complicated geometry of the surface coil, experiments were performed on single loops tuned to the Larmor frequency at 3.0T. The loop size selected for the experiment was based on the mode short from the two probe tuning fixture discussed in Section 3. This specific geometry was selected because it is tuned to the Larmor frequency of 127.72 MHz. This was verified by first inserting the loop into the simulation model, and measuring the coupling between the two drive points on the body coil. In Figure 19 it can be seen that the resonance is split around 127.72 MHz indicating the loop is tuned to same resonant frequency as the coil.

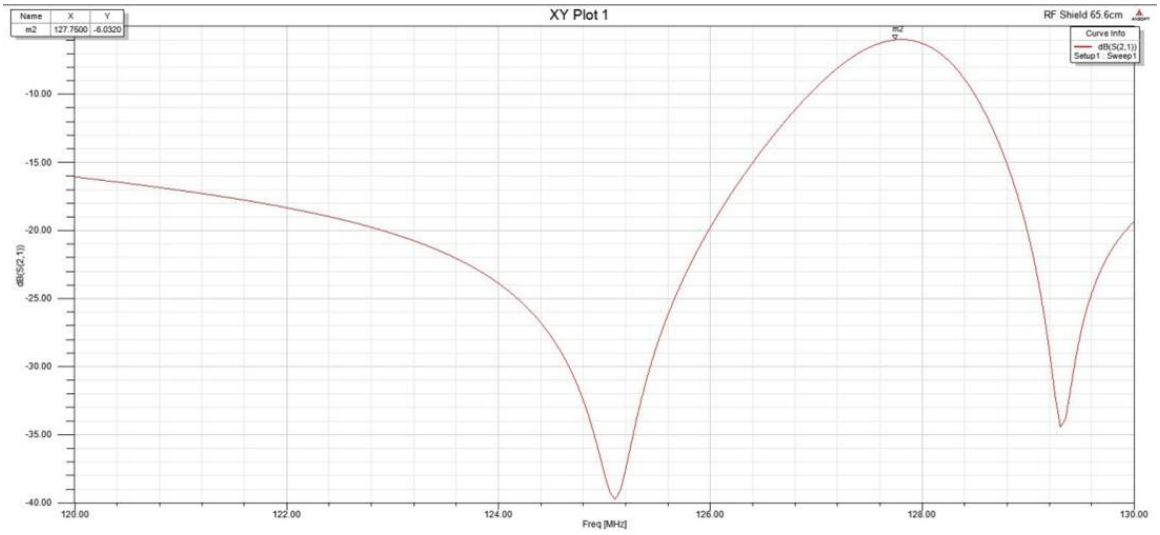

Figure 19: Body coil S21 parameter with tuned resonant loop present.

The tuning loop is 20 cm x 40 cm and is constructed of 1 cm wide 3M copper tape. The loop has six discrete capacitors spaced along it. The details of the tuning loop design are given in Figure 20.

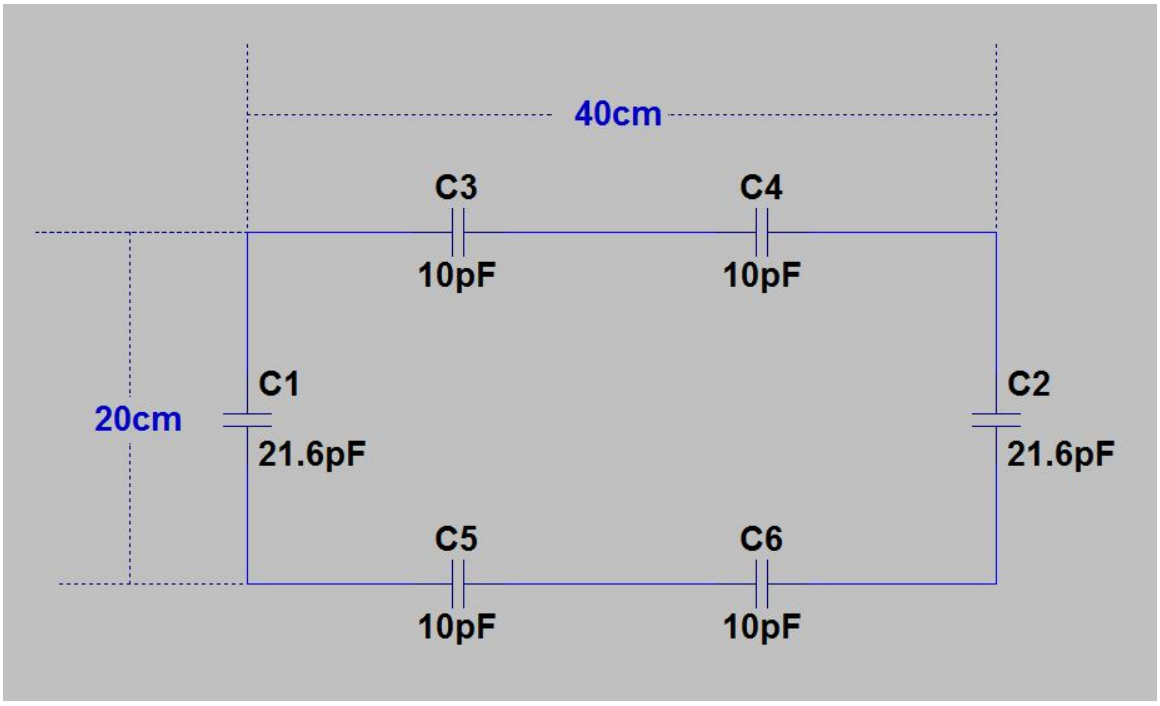

Figure 20: Tuning loop design details.

The first step in setting up the simulations was to determine how many, and of what

value, resonant tanks be implemented in the circuit. C1 and C4 were the natural choices for tank locations, since they had different capacitor values than the other four capacitors. However, the decision of how many tanks to implement, still had to be made. An arbitrarily low impedance value of 1.8 Ω/cm^2 of blocking was chosen to test versus infinite blocking. A parallel LC tank providing an inductive reactance of 1440 Ω was implemented at C1. For the infinite case, C1 was simply removed creating a true open circuit at that location. Figure 21 shows the resulting B_1 maps from the two experiments, with the inductive block on the left and the infinite block on the right.

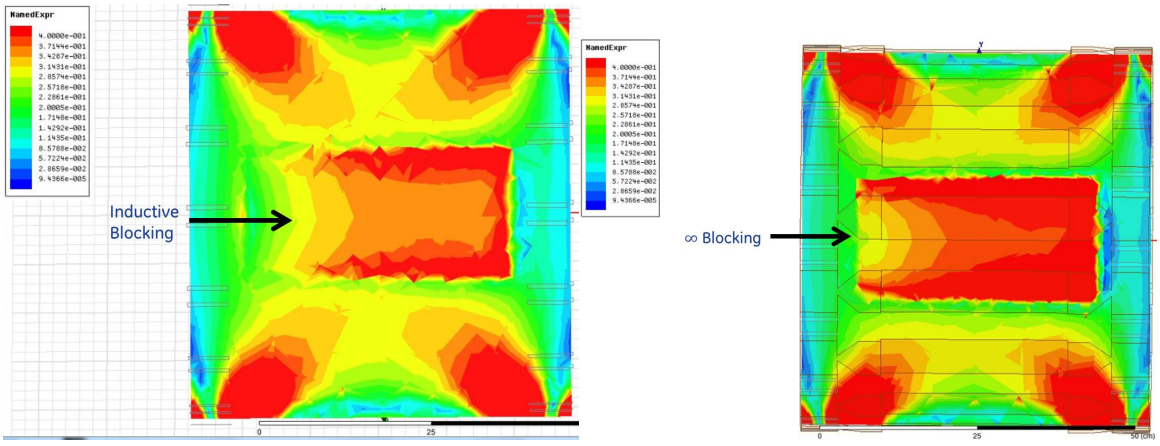

Figure 21: B_1 maps for a single inductive and a single infinite block on a large resonant loop.

The figure makes it apparent that the inductive block is more effective at reducing B_1 distortions. It also shows that another blocking location may be desirable to further reduce the distortion. A second resonant tank was added at C4 with the same inductive reactance as the first tank. Figure 22 illustrates that the B_1 distortion again improves, and again appears to be better than two infinite blocks, although the difference is less than in the single block case.

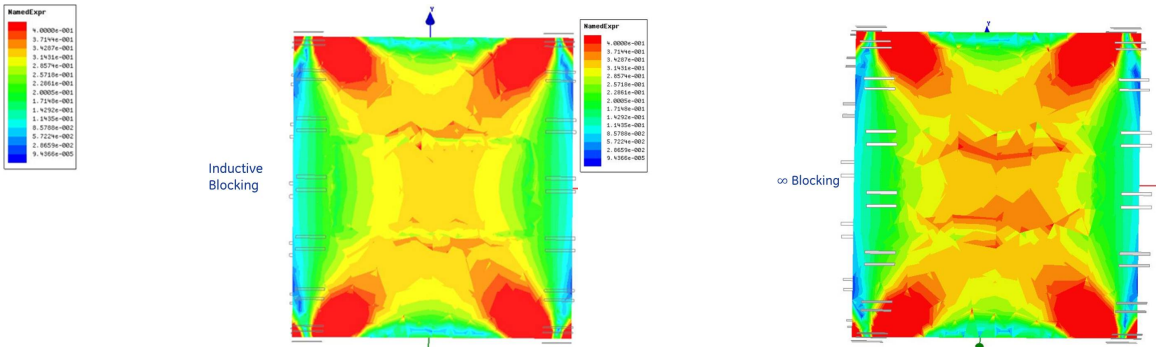

Figure 22: B_1 maps for dual inductive and dual infinite blocks on a large resonant loop.

Based on the above results it was decided to move forward with two blocks per loop configuration. With only two data points for blocking values the next step was to try and determine the optimal blocking for a loop of this size. First a plot of the imaginary portion of the impedance (reactance) versus inductor value for a parallel LC circuit was created based on (19), (20), (21), with C = 21.6 pF. The plot was concentrated around the resonance condition and is shown in Figure 23.

$$Z_C = \frac{1}{j\omega C} \tag{19}$$

$$Z_L = j\omega L \tag{20}$$

$$Z_{Tank} = -j\left(\frac{\omega L}{\omega^2 LC - 1}\right) \tag{21}$$

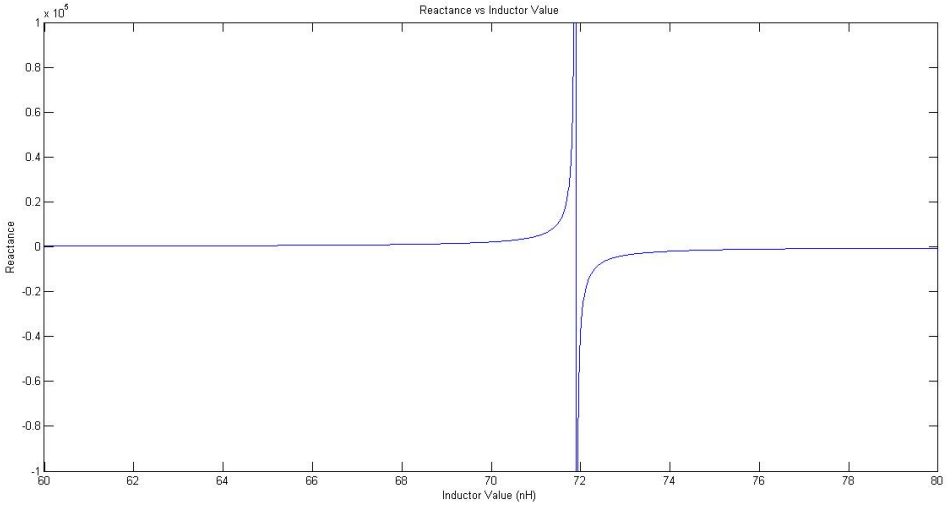

Figure 23: Reactance versus inductor value for a parallel LC tank with C=21.6 pF.

From this plot a set of inductor values were selected to be tested. These inductor values, their corresponding tank impedance, and overall loop impedance are detailed in Table 7. The table also details the average surface current induced in the loop at each blocking value. Since induced current is related to B_1 created by the body coil, an effort was made to normalize the B_1 seen by each loop, by adjusting the body coil drive power until $B_{ave}$was equal for every situation according to (22). The elliptical surface was 45 cm in the z-direction and 50 cm in the x-direction, located at a position 5mm above the loop. Note that tanks resonance occurs when L ~ 78.89 nH for C = 21.6 pF.

$$B_{ave} = \iint_{ellipse} \mathbf{B} \cdot d\mathbf{s} \tag{22}$$

L_{val} (nH)	X_{block}(ohms)	X_{loop}(ohms)	J_{ave}(A/m)
60	291.1	582.2	0.459074353
65	544.2	1088.4	0.237964519
68	1008.5	2017	0.121445683
68.5	1165.7	2331.4	0.114787558
69	1377.4	2754.8	0.10832228
69.5	1677.6	3355.2	0.104695161
70	2136.7	4273.4	0.104323645
70.5	2926	5852	0.106040092
71	4602.1	9204.2	0.113983374
71.5	10576	21152	0.119078045
71.89	120000000	240000000	0.124528534
72	-37773	-75546	0.128743054
72.5	-6857.1	-13714.2	0.142595043
75	-1391.3	-2782.6	0.227821507
80	-569.1	-1138.2	0.507101019

Table 7: Induced surface current versus LC tank blocking values for a large resonant loop.

In this simulation it is clear that induced current is minimized not when the LC blocks are at resonance, but rather with an inductive impedance of 2146.7 ohms each. However, as stated previously, simply minimizing surface current may not be enough when complex geometries are introduced. Therefore the loop was also evaluated using the modified NEMA PDNU parameter. This evaluation also removed the dependence on drive strength, since the parameter is a ratio of the field within a single configuration. For the modified NEMA PDNU analysis, the same rectangular plane used in Section 3 was used here, and the results are detailed in Table 8. Again the B_1 uniformity is maximized for an inductive impedance of 2146.7 ohms per resonant block. For reference Figure 24 shows the B_1 comparison maps of the maximum B_1 uniformity and the infinitely reactive blocking condition respectively.

L_{val} (nH)	X_{block}(ohms)	X_{loop}(ohms)	PDNU(%U)
60	291.1	582.2	2.64
65	544.2	1088.4	23.65
68	1008.5	2017	52.99
68.5	1165.7	2331.4	55.15
69	1377.4	2754.8	56.73
69.5	1677.6	3355.2	57.67
70	2136.7	4273.4	58.17
70.5	2926	5852	57.26
71	4602.1	9204.2	56.19
71.5	10576	21152	55.16
71.89	120000000	240000000	54.70
72	-37773	-75546	53.10
72.5	-6857.1	-13714.2	49.92
75	-1391.3	-2782.6	33.06
80	-569.1	-1138.2	7.79

Table 8: Modified NEMA PDNU versus LC tank blocking values for a large resonant loop.

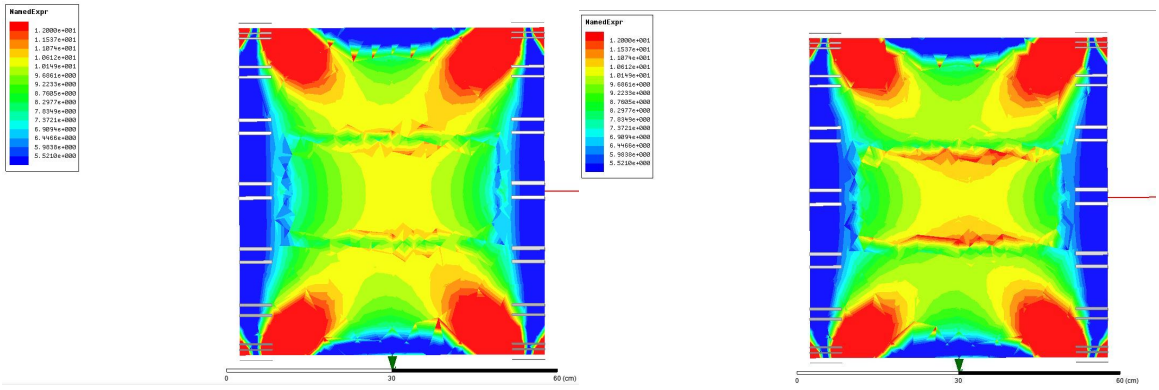

Figure 24: B_1 map for LC tanks producing the maximum modified NEMA PDNU value versus the infinite reactance blocking tank.

The above plots show that during the infinite blocking condition, the secondary B_1 being generated is adding to the primary B_1 inside of the loop, while taking away from it outside the loop. With the inductive 2146.7 ohm per block, the disturbance is much less pronounced, and seems to be balanced over the loop conductors themselves, indicating a less cohesive current flow in the loop. In order to verify this theory, a surface vector plot of each loop was created in Figure 25, with the inductive block on the left, and the

infinite block on the right. It appears that the infinite block is allowing a stronger current loop to flow on the inside edge of the conductor.

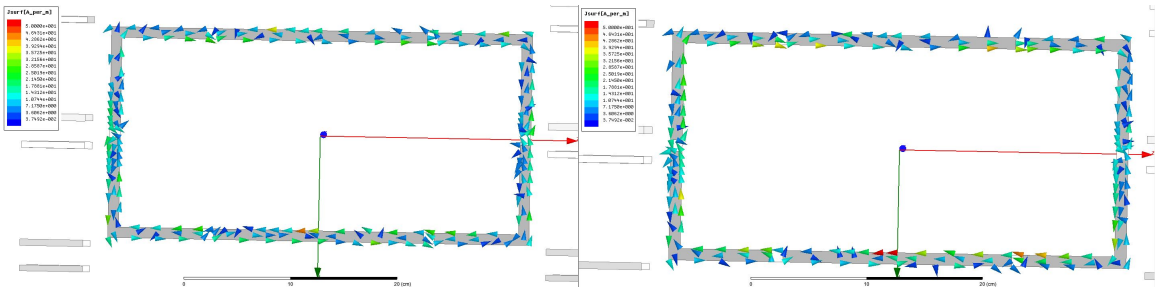

Figure 25: Surface current vector map for LC tanks producing the maximum modified NEMA PDNU value versus the infinite reactance blocking tank.

This phenomenon is explained in Figure 26. If Z_1 and Z_2 are infinite blocking impedances, i_1 and i_2 will be entirely lossless current loops (neglecting conductor resistivity). However, on the inside edge of the conductor i_1 and i_2 create loop i_3. Similarly i_4 is created on the outside by the same phenomenon. If Z_1 and Z_3 have a finite impedance, some of i_1, and some of i_2 will transfer through the impedance to the other loop, losing energy along the way. This reduces the magnitude of the current seen by i_3 and i_4, which results in lower field disturbances.

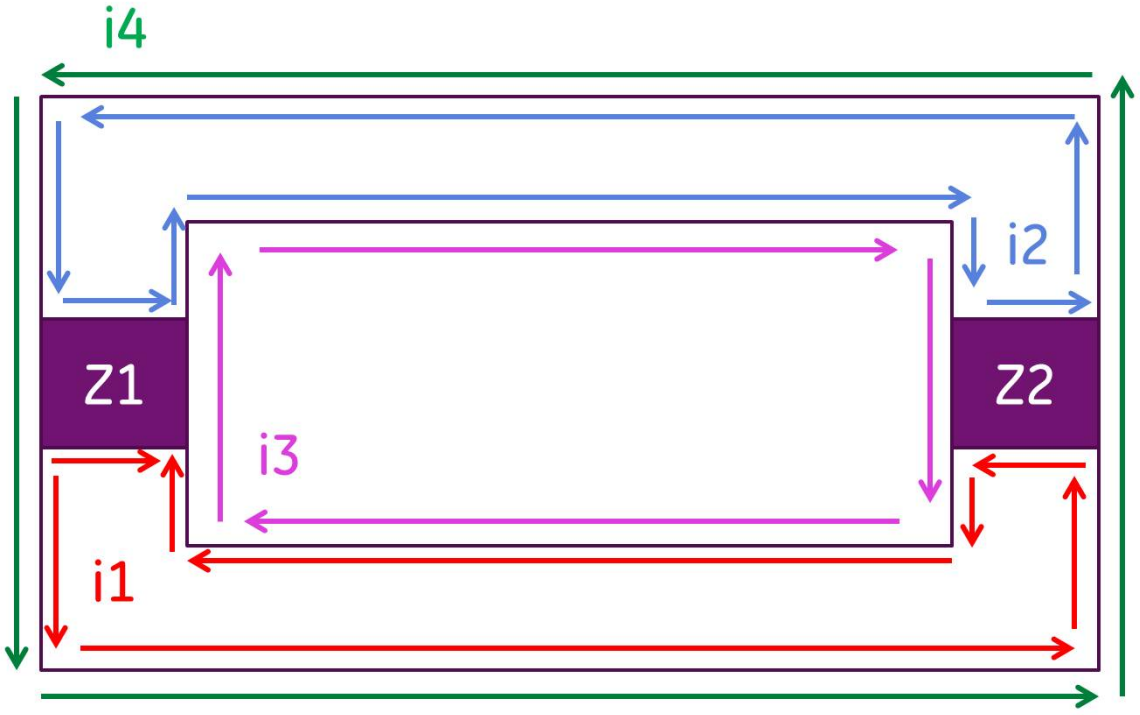

Figure 26: Diagram of induced currents on a large resonant loop with two blocking locations.

4.3 Small Loop Experiment

In order to ascertain the dependence of the above result on loop size the same experiment was repeated for a small sized tuning loop more representative of the loop size in the surface coil. The loop was again tuned to 127.72 MHz and its design details are shown in Figure 27. For simplicity the small loop had distributed capacitors of equal value on the loop, and the tank locations were left along the system Z-axis.

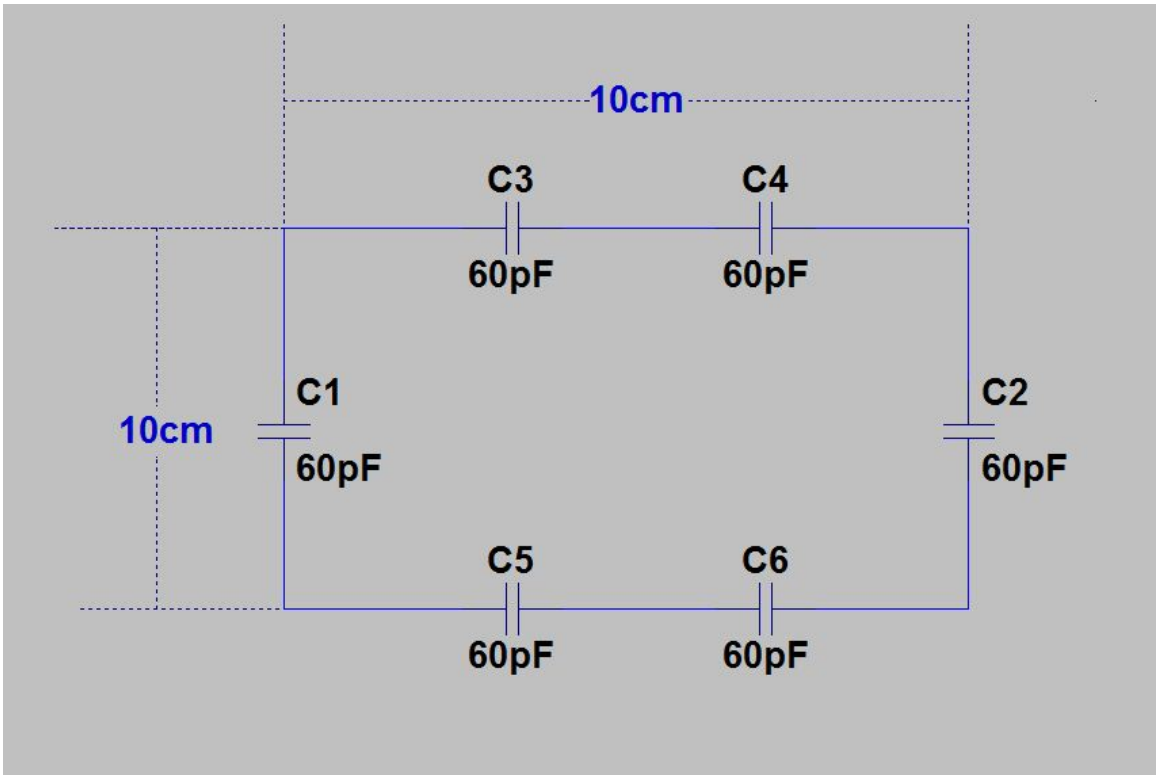

Figure 27: Small resonant loop design details.

Table 9 details the results from the small loop experiment.

L_{val} (nH)	X_{block}(ohms)	X_{loop}(ohms)	J_{ave}(A/m)	PDNU(%U)
13.99	24.43	48.87	0.106276774	21.4545
18.99	57.23	114.47	0.076349107	50.058
21.99	117.39	234.78	0.048275094	64.529
22.49	137.77	275.54	0.045354907	64.5201
22.99	165.19	330.38	0.04233898	64.5113
23.49	204.09	408.18	0.039771808	64.5021
23.99	263.56	527.13	0.037655155	64.493
24.49	365.81	731.62	0.036660403	64.4984
24.99	582.88	1165.78	0.034396025	64.4921
25.49	1356.00	2712.00	0.033622134	64.467
25.88	1303200.00	2606400.00	0.03259011	64.4672
25.99	-4925.60	-9851.2	0.032468417	64.4656
26.49	-902.52	-1805.04	0.032461859	64.456
28.99	-193.62	-387.24	0.040960688	57.8395
33.99	-87.05	-174.10	0.100240477	35.3826

Table 9: Induced surface current and modified NEMA PDNU versus LC tank blocking values for a small resonant loop.

4.4 Desired Blocking versus Loop size

It must be noted that in the above results the sampling plane was not adjusted in size to match the loop of interest. This causes the smaller loop sizes to have their results dominated by the undisturbed field in the body coil making the disturbances less apparent. Nonetheless both data sets show a strong correlation, the large loop indicating a value of 5.34 Ω/cm^2, and the small loop a value of 2.34 Ω/cm^2 for a single loop. Figure 28 shows the plots of the two different data sets with the lower B_1 valued end points removed. The next step is to apply the solution to the existing problem with the surface coil.

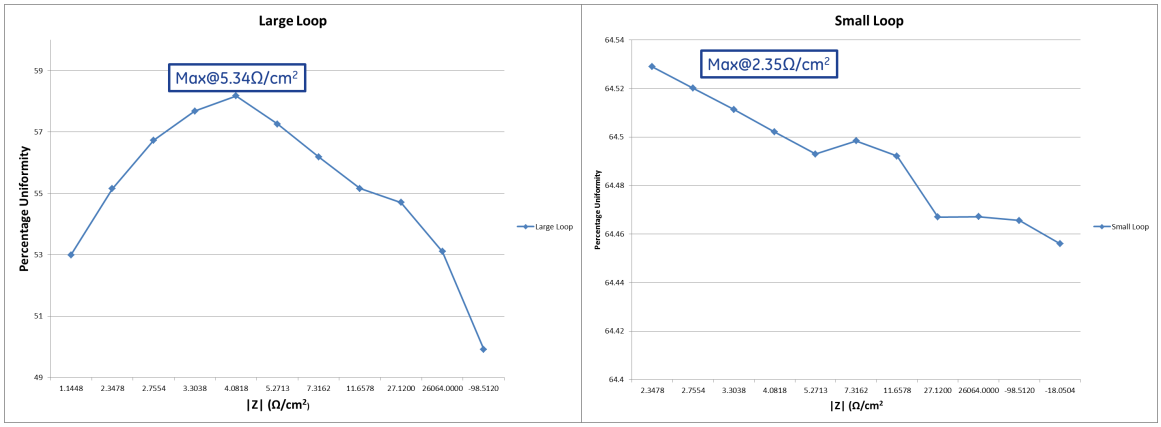

Figure 28: Modified NEMA PDNU versus impedance per loop for a large resonant loop and small resonant loop.

5 Solution Demonstration

5.1 Application of Solution with Current Blocking Locations

The results achieved in Section 4 show B_1 distortion improvement for single decoupled loops in an MRI system. The next logical step is to apply the results from Section 4 to the surface coil to see if improvements over the existing blocking scheme can be made. In order to simplify the solution, the decision was made to attempt to keep the blocking locations in the same quantity and locations used by the existing scheme. By keeping locations the same, implementing the solution practically would only require an inductor value change, and no other change to the blocking topology of the surface coil. Since two different values were calculated in Section 4, depending on loop size, both values will be checked on the existing surface coil.

The first investigation was done with an inductive blocking value of 5.34 Ω/cm^2, with two blocking locations on very loop. The details of the blocks are shown in Table 10 .

Loop	Size (cm^2)	Z_{total} (ohms)	Z_{block} (ohms)	L_{tank} (μH)
Loop 1	129.3	737.1	368.55	72.63
Loop 2	163.8	933.9	466.95	75.13
Butterfly	244	1390.8	695.4	78.46

Table 10: Inductive block details for 5.34 Ω/cm^2 application to surface coil loops.

The resulting B_1 maps can be seen in Figure 29. A comparison to the maps created by the existing blocking scheme appear to show that the inductive blocking scheme performs more poorly than the existing scheme. This qualitative conclusion is confirmed by looking at the modified NEMA PDNU, which is is an extremely low 6.47% for this configuration.

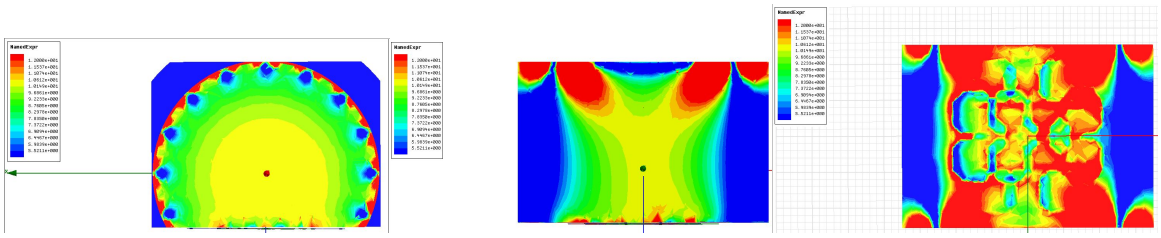

Figure 29: B_1 maps for 5.34 Ω/cm^2 inductive blocking, implemented at the existing blocking locations. Images show the axial, sagittal, and surface coil coronal planes respectively

A closer look at the images shows the secondary B_1 field is adding to the primary B_1 outside of the loops, while taking away from the primary B_1 inside the loops. This is a strong indication that the reactive portion of the impedance is too low in magnitude, and inductive in nature. This was confirmed by dropping the impedance values of the blocks to match the 2.34 Ω/cm^2 result achieved in Section 4.3. With the blocks set to 2.34 Ω/cm^2 a modified NEMA PDNU value of 2.5% was achieved. The B_1 maps with the lower blocking values, shown in Figure 30, show a more dramatic effect of the secondary B_1 adding outside of the loops, and taking away from the primary B_1 inside of the loops.

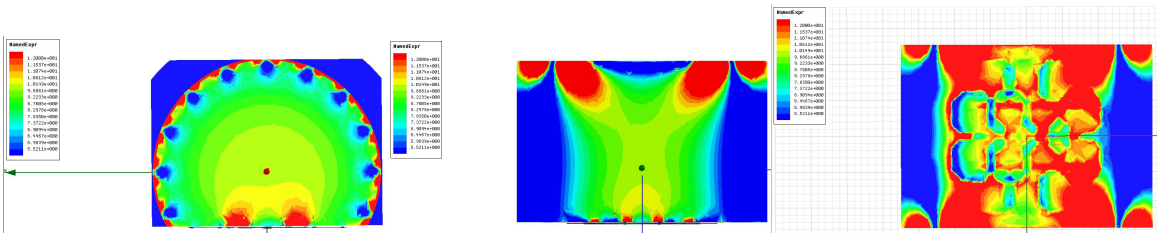

Figure 30: B_1 maps for 2.34 Ω/cm^2 inductive blocking, implemented at the existing blocking locations. Images show the axial, sagittal, and surface coil coronal planes respectively

5.2 Application of Solution with new Blocking Locations

After reviewing the results from Section 5.1 another experiment was run with new blocking locations. These locations were chosen based on the arguments from Dr. Boskamp and Dr. Goldhaber [13], that parasitics create unaccounted for loops in the complex geometry of the surface coil. A discussion with Dr. Selaka Bulumulla and Dr. Saikat Saha gave some direction on choosing decoupling locations. The theory in controlling the currents in multiple loops, has to do with balancing the current between all loops created by the parasitic capacitances between each loop. The theory is similar to what is shown in Figure 26, but is re-illustrated in Figure 31 for clarity. Even if each loop is opened to an infinite impedance, the parasitics between the loops will still create an outer loop of current, in phase with the excitation field. Inductive blocking on each loop causes the inner loop to be 180° out of phase with the outer loop. If the currents between the two loops can be adequately balanced, the total current in the system can be minimized. Obviously this gets more complicated as the array structure, and the number of overlaps grows, but it gives a starting point.

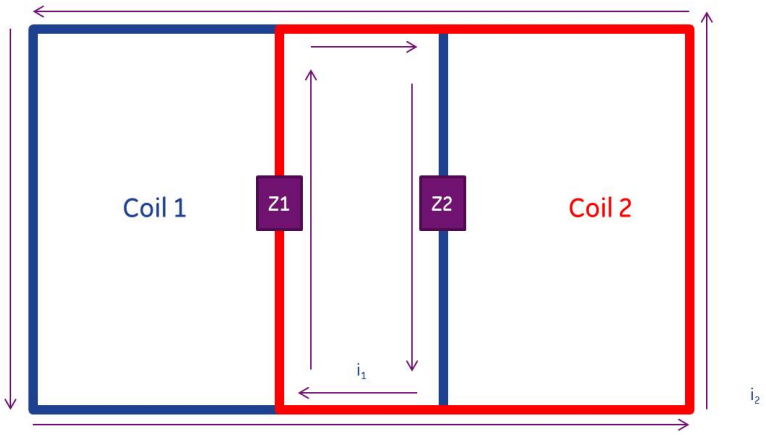

Figure 31: Current sharing diagram for two overlapped resonant loops.

Based on this new blocking locations were selected, and the number of blocks were reduced to one block per single loop, and maintaining the existing two blocks per butterfly loop. The single blocks carried a value of 5.75 Ω/cm^2, while the butterfly loops were blocked at 11.5 Ω/cm^2. The reason a higher impedance is chosen for the butterfly loops, is due to their more complicated geometry and crossed conductors. Additionally, the images in Section 5.1 show the strongest distortions are caused by the butterfly loops. Because of this, the small scale experiments are less likely to apply and higher blocking was chosen, but kept finite in order to attempt a current balance as described in Figure 31.

Figure 32 shows the empty B_1 in the surface coil coronal plane, the B_1 with surface coil present, the B_1 with the new blocking locations and infinite impedance at each block, and B_1 with the inductive blocking scheme over the same FOV. Figure 33 shows the same configurations in the axial plane, and Figure 34 shows the same configurations for the sagittal plane. Figures 32, 33, and 34 all have the empty condition in the top left, the surface coil in the top right, the newly located infinite blocks in the bottom left, and the newly located inductive blocks in the bottom right. The pictures show that that inductive blocking at the new locations appears to perform better than the infinite blocking at the new locations. It appears as though it performs similarly to the standard surface coil

blocking from an image uniformity perspective, but is hard to tell, especially since all images are normalized to the surface coil coronal plane.

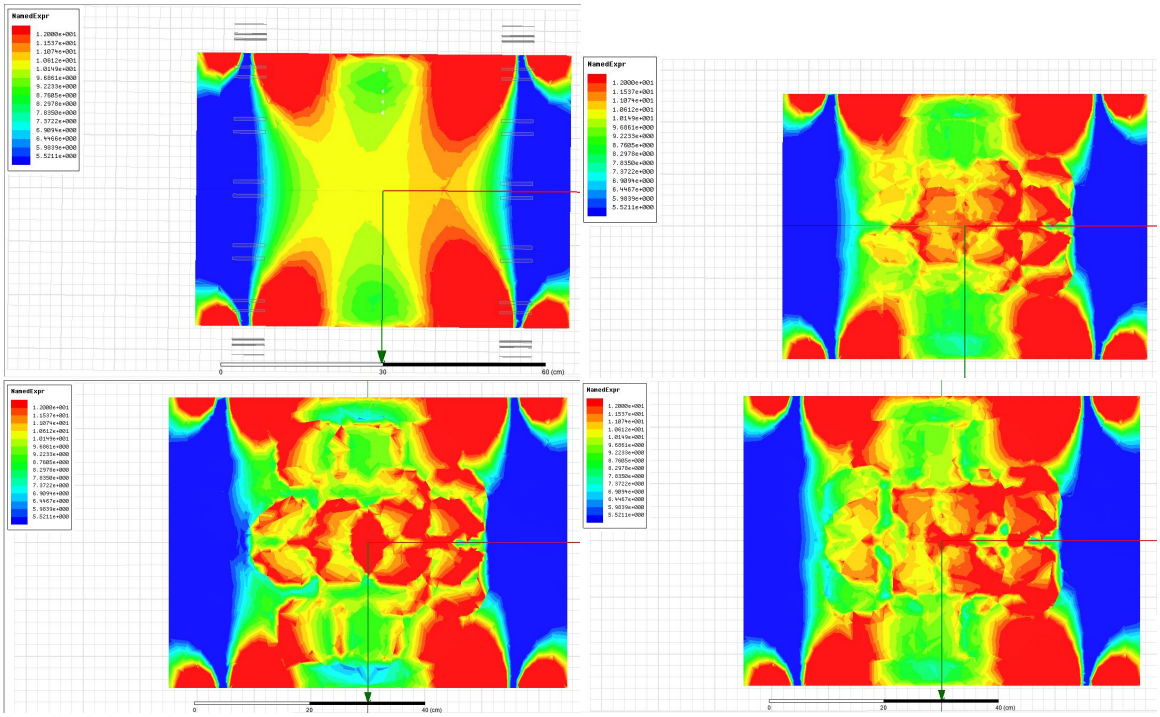

Figure 32: B_1 maps in the surface coil coronal plane for the empty condition, the existing surface coil blocking scheme, a reduced number of inductive blocks, and a reduced number of infinite blocks clockwise from top left.

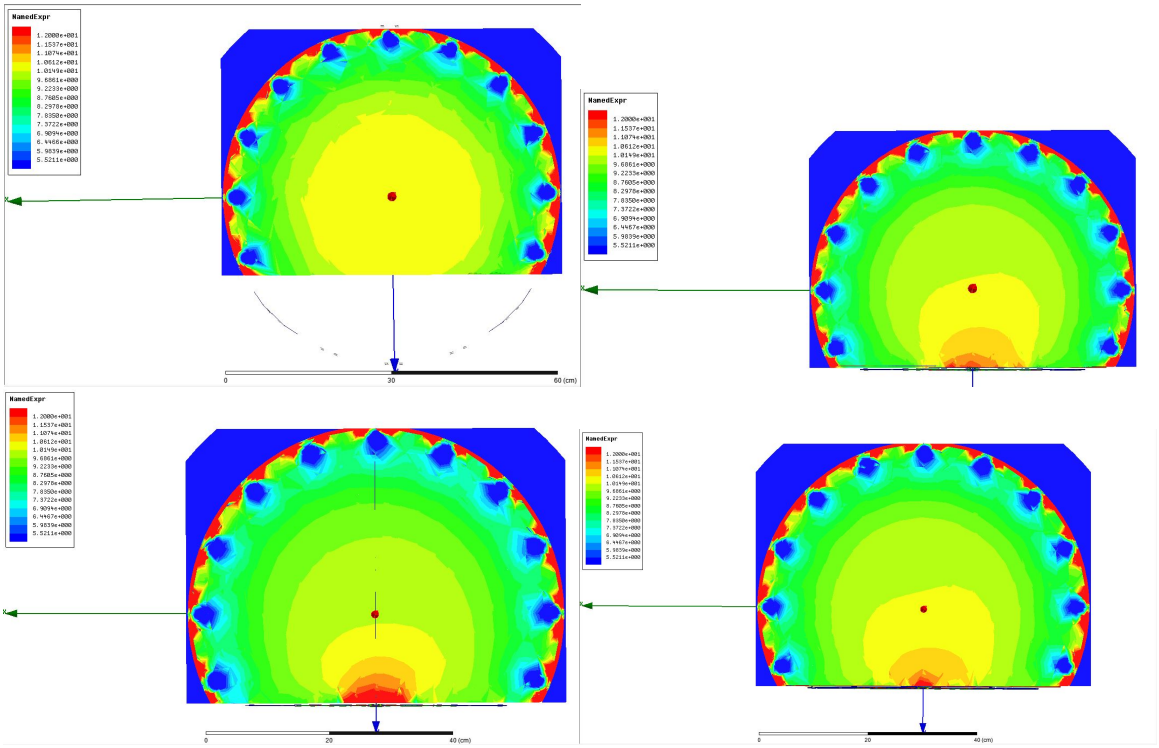

Figure 33: B_1 maps in the axial plane for the empty condition, the existing surface coil blocking scheme, a reduced number of inductive blocks, and a reduced number of infinite blocks clockwise from top left.

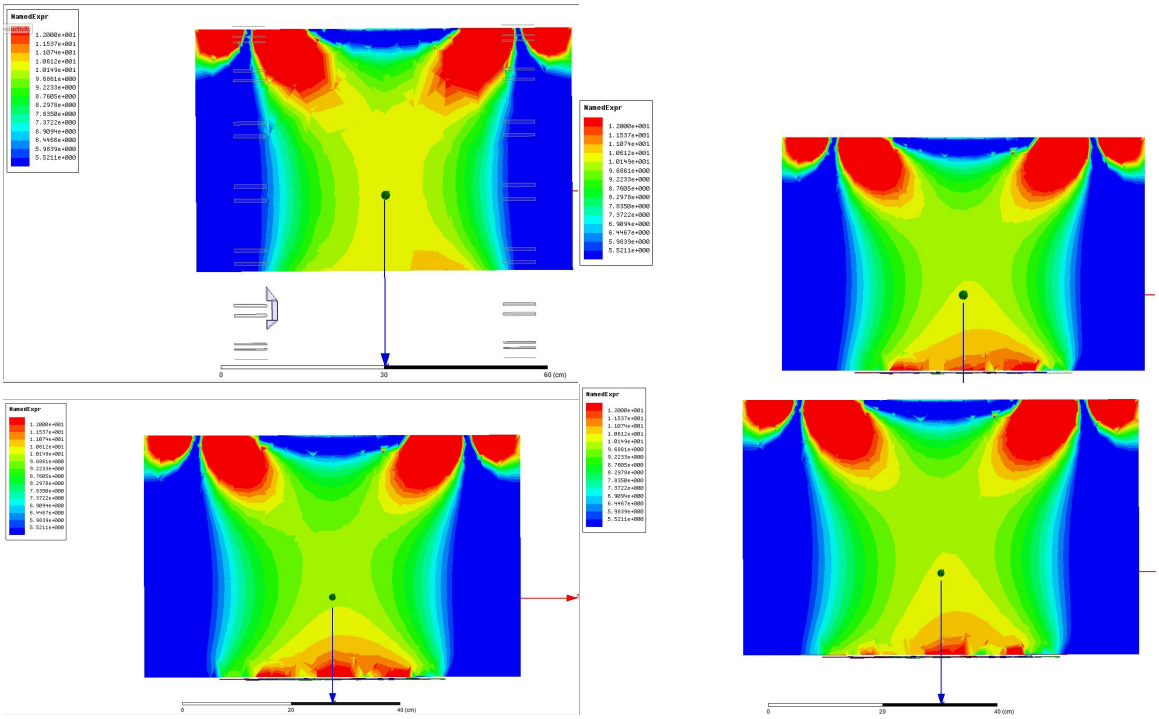

Figure 34: B_1 maps in the Sagittal plane for the empty condition, the existing surface coil blocking scheme, a reduced number of inductive blocks, and a reduced number of infinite blocks clockwise from top left.

Again it should be noted when with the updated blocking locations the total number of blocks was reduced by 10, from 28 to 18. With the reduced number of blocking locations, the improvement in body coil drive port isolation between infinite blocking, and inductive blocking is evident. Figure 35 shows the simulated S21 plots of the standard surface coil, reduced infinite blocking, and of the reduced inductive blocking respectively. It is quite clear from the plots that at the resonant frequency, inductive blocking provides a further 2.47dB of isolation over the infinite blocks at the same locations, which is another strong indicator that the body coil and surface coil are coupling less. It can be seen that the isolation with reduced inductive blocking, is very close to the isolation provided with the standard blocking scheme, -16.33dB versus -16.99dB respectively.

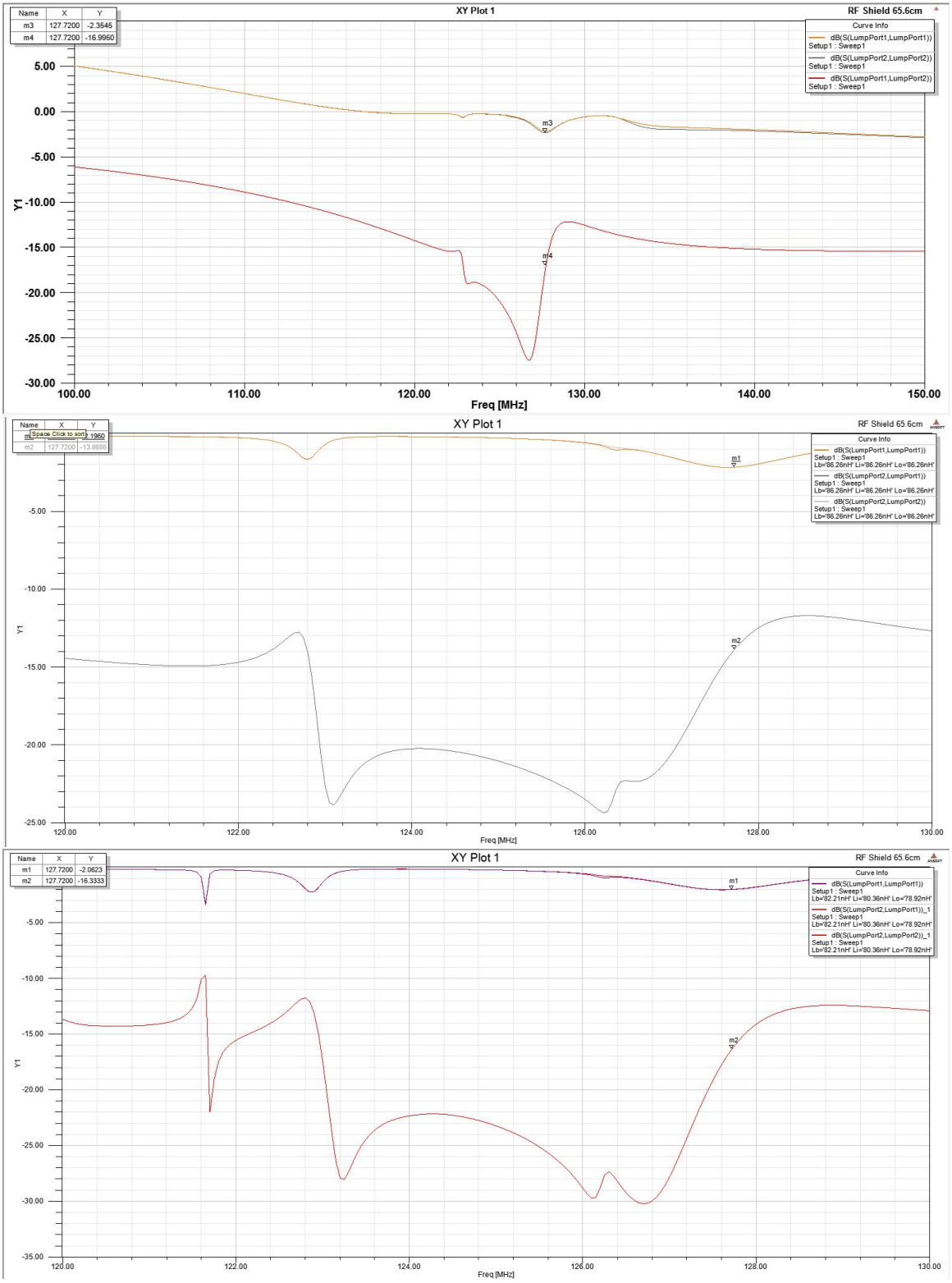

Figure 35: Simulated S21 parameter for the standard surface coil, surface coil with a reduced number of infinite blocks, and a reduced number of inductive blocks at the same locations.

The modified NEMA PDNU numbers are summarized in Table 11 below. It is clear from the numbers that in the reduced configuration, the inductive blocking performs much better than the traditional infinite LC tank. Additionally the inductive blocking slightly outperforms the current surface coil configuration with 10 less blocking locations. Table 12 shows how the performance numbers change when an elliptical FOV is adopted, which is more reflective of what is used in the actual system. It shows the reduced inductive blocking greatly outperforms the standard surface coil scheme when the elliptical FOV is adopted.

	Empty	Surface coil	Reduced ∞ Blocking	Reduced Ind Blocking
NEMA PDNU	43.41%	30.39%	27.28%	32.63%

Table 11: Blocking Scheme Comparisons

	Empty	Surface coil	Reduced ∞ Blocking	Reduced Ind Blocking
NEMA PDNU	56.25%	28.36%	21.58%	39.87%

Table 12: New Blocking Scheme with Elliptical FOV

6 Conclusions and Future Work

6.1 Conclusions

It has clearly been demonstrated that blocking networks with an inductive impedance show the ability to provide better B_1 uniformity than traditional infinite blocks, even when the number of blocking networks are reduced. There are several physical principals at play which favor inductive impedance over infinite blocking, including field loops, and parasitic effects in complex phased arrays. The application of inductive blocking was first demonstrated on a single large loop placed at iso-center of the coil. It was then confirmed using a smaller single loop at the same position. The second experiment also showed that the optimal blocking impedance per loop area, seemed to change as loop size changed.

The application was then performed at the existing blocking locations on the surface coil. This application showed a much poorer performance than the standard infinite reactance blocking in the existing surface coil. The B_1 maps in this configuration showed too much current, 180 degrees out of phase with the excitation current, was flowing in the surface coil loops. After this new blocking locations were chosen for the non-butterfly loops in the coil. The new locations were chosen on the principal of current sharing, and the value of the blocks were slightly higher than those predicted by the large loop experiment. The butterfly loops locations were kept the same, and the values increased in an attempt to reduced the impact the butterfly loops had on B_1 distortion. However, the values were kept finite to still allow the current sharing principle to work. With the new locations and values, an improvement in B_1 distortion was observed. This result is made more promising by the fact that the number of blocking networks were reduced by 35%, indicating that in the future there is a lot of room for optimization.

6.2 Future Work

As MRI technology continues to advance, and image quality becomes more and more critical, B_1 uniformity will continue to get more attention during development phases. It would be advantageous to continue to develop and optimize phased array decoupling techniques. This work provides a good basis by showing that inductive decoupling may prove a better alternative to standard decoupling techniques.

Moving forward there is a lot of opportunity for optimization of the inductive decoupling scheme demonstrated here, both for single loop and phased array applications. In the single loop application, more work studying the dependence of optimum reactive impedance on loop conductor dimensions would prove beneficial. Also looking at loop position in the primary B_1 field may provide a more robust engineering principle which can be followed. In the phased array application, further study of the current sharing principle could provide the most improvement over the work of this paper. Specifically, a study of

how parasitic effects change optimal values as phased arrays grow in complexity would be a very logical next step.

References

[1] Guclu, C., Venkatraman, S., Hornblad, A., & Maier, J. (1999). The Effect of Blocking Network Impedance on the Bl Field Distortion in the Phased-Array Coils.ăProc. Intl. Soc. Mag. Reson. Med,ă2071-2071. Retrieved May 7, 2014, from http://cds.ismrm.org/ismrm-1999/PDF7/2071.pdf

[2] Collins, C., & Wang, Z. (2011). Calculation of radiofrequency electromagnetic fields and their effects in mri of human subjects. Magnetic Resonance in Medicine, 65(5), 1470-1482. doi: 10.1002/mrm.22845

[3] Dowell, N. G. and Tofts, P. S. (2007), Fast, accurate, and precise mapping of the RF field in vivo using the 180ř signal null. Magn Reson Med, 58: 622630. doi: 10.1002/mrm.21368

[4] M A Bernstein, K F King and X J Zhou (2004). Handbook of MRI Pulse Sequences. San Diego: Elsevier Academic Press. p. 960. ISBN 0-12-092861-2.

[5] Chin, C., & Smith, M. (1998). Circular and elliptical birdcage coil design for magnetic resonance imaging. In IEEE 24th annual northeast bioengineering conference (pp. 26-28). doi: 10.1109/NEBC.1998.664866

[6] Watkins, J., & Fukushima, E. (1988). Highpass birdcage coil for nuclearmagnetic resonance. Review of Scientific Instruments, 59(6), 926-929. doi: 10.1063/1.1139751

[7] Vaughan, J. (2012). Quadrature Surface Coils. In RF coils for MRI. Chichester: Wiley.

[8] Taracila, V., Chan, P., & Robb, F. (2010). Minimal acceptable blocking impedance for rf receive coils. Proc. Intl. Soc. Mag. Reson. Med, 18, 3928. Retrieved from http://cds.ismrm.org/protected/10MProceedings/files/3928_4994.pdf

[9] Chu, D., Matis, R., Lindsay, S., Stormont, R., Boskamp, E., & Kurucay, S. (2009). Minimal acceptable blocking impedance for rf receive

coils. Proc. Intl. Soc. Mag. Reson. Med, 17, 4730. Retrieved from http://cds.ismrm.org/protected/09MProceedings/files/04730.pdf

[10] Kocharian, A., Rossman, P., Hulshizer, T., Felmlee, J., & Riederer, S. (2000). Determination of appropriate rf blocking impedance for mri surface coils and arrays. Magnetic Resonance Materials in Physics, Biology and Medicine, 10(2), 80-83. Retrieved from http://link.springer.com/article/10.1007/BF02601842

[11] Liu, W., Collins, C., Delp, P., & Smith, M. (2004). Effects of end-ring/shield configuration on homogeneity and signal-to-noise ratio in a birdcage-type coil loaded wth a human head. Magnetic Resonance in Medicine, 2004(1), 217-221. Retrieved from http://onlinelibrary.wiley.com/doi/10.1002/mrm.10683/abstract

[12] National Electrical Manufacturers Association (NEMA). (2007) Determinaiton of image uniformity in diagnostic magnetic resonance images. NEMA Standards Publication MS3-2008. Rosslyn, VA

[13] Boskamp, E., & Goldhaber, D. (2014, May). B1 distortion by residual currents in decoupled receive arrays. Abstract Joint annual meeting ismrm-esmrmb, Milan, Italy. Retrieved from http://www.ismrm.org/14/program_files/TP04.htm

[14] Dabirzadeh, A. (2008). Rf coil design for multi-frequency magnetic resonance imaging and spectroscopy. (Unpublished master's thesis). Retrieved from http://repository.tamu.edu/handle/1969.1/ETD-TAMU-3157?show=full